



### **Science Arts & Métiers (SAM)**

is an open access repository that collects the work of Arts et Métiers Institute of Technology researchers and makes it freely available over the web where possible.

This is an author-deposited version published in: <https://sam.ensam.eu>  
Handle ID: [.http://hdl.handle.net/10985/20502](http://hdl.handle.net/10985/20502)

#### **To cite this version :**

Camille GOUIN, Carlos JUNQUEIRA-JUNIOR, Eric GONCALVES DA SILVA, Jean-Christophe ROBINET - Numerical investigation of three-dimensional partial cavitation in a Venturi geometry - Physics of Fluids - Vol. 33, n°6, p.063312 - 2021

Any correspondence concerning this service should be sent to the repository

Administrator : [scienceouverte@ensam.eu](mailto:scienceouverte@ensam.eu)



# Numerical investigation of three-dimensional partial cavitation in a Venturi geometry

doi: [10.1063/5.0052913](https://doi.org/10.1063/5.0052913)

Camille Guoin,<sup>1,a)</sup>  Carlos Junqueira-Junior,<sup>1</sup>  Eric Goncalves Da Silva,<sup>2</sup>  and Jean-Christophe Robinet<sup>1</sup> 

## AFFILIATIONS

<sup>1</sup>DynFluid Laboratory, ENSAM, 151 Boulevard de l'Hôpital, 75013 Paris, France

<sup>2</sup>Institut Pprime, UPR 3346 CNRS, ISAE-ENSMA, 1 Avenue Clément Ader, 86961 Futuroscope Chasseneuil Cedex, France

<sup>a)</sup> Author to whom correspondence should be addressed: [camille.psb@hotmail.fr](mailto:camille.psb@hotmail.fr)

## ABSTRACT

Sheet cavitation appears in many hydraulic applications and can lead to technical issues. Some fundamental outcomes, such as, the complex topology of 3-dimensional cavitation pockets and their associated dynamics need to be carefully visited. In the paper, the dynamics of partial cavitation developing in a 3D Venturi geometry and the interaction with sidewalls are numerically investigated. The simulations are performed using a one-fluid compressible Reynolds-averaged Navier–Stokes solver associated with a nonlinear turbulence model and a void ratio transport equation model. A detailed analysis of this cavitating flow is carried out using innovative tools, such as, spectral proper orthogonal decompositions. Particular attention is paid in the study of 3D effects by comparing the numerical results obtained with sidewalls and periodic conditions. A three-dimensional dynamics of the sheet cavitation, unrelated to the presence of sidewalls, is identified and discussed.

## I. INTRODUCTION

Cavitation is the formation of vapor cavities in a liquid due to a pressure drop. The phenomenon occurs in hydraulic systems or turbomachinery and can, eventually, cause structural damage and noise and degrade the performance of the apparatus. Such effects drive the study of the different types of cavitation, and, in particular, considerable efforts have been made to explore the dynamics of partial cavities appearing along solid bodies. Such cavitation pockets are characterized by a fluctuating closure region leading to cavity length oscillations and the shedding of vapor structures. Partial cavity can be classified in two main forms of appearance: closed or quasi-stable cavity and open cavity or cloud cavitation, depending on the flow in the cavity closure region.<sup>1</sup> A quasi-stable cavity presents only small shedding at its closure region with a relatively stable cavity length. In opposite, cloud cavitation is a highly unsteady phenomenon presenting a periodically varying length that is associated with the large shedding of vapor clouds. Both types of cavities have been studied, experimentally and numerically, to describe the physical mechanism, the internal structure of cavities, the turbulence–cavitation interaction and to investigate the transition from quasi-stable to cloud cavitation.<sup>2–10</sup> Two main mechanisms have been identified for the break-off cycles: the development of a liquid re-entrant jet and the propagation of pressure waves created by the cloud collapses.<sup>11–15</sup>

The structures of partial cavities have a fully three-dimensional topology as observed on hydrofoils with high-speed imaging method. The re-entrant jet does not progress only on the streamwise direction, and a spanwise component was depicted.<sup>16</sup> To distinguish between various directions of the re-entrant flow, the term side-entrant jet was introduced. This term refers to the part of the jet that has a strong spanwise velocity component directed into the cavity originating from the sidewalls. The term re-entrant jet or middle jet is reserved for the flow originating from the part of the cavity where the closure is more or less perpendicular to the incoming flow and is thus mainly directed upstream. Foeth *et al.* (2006)<sup>17</sup> investigated the cavitating flow structures on the Delft twisted hydrofoil and reported the joint action of the re-entrant and side-entrant jets in the shedding. Dular *et al.* (2007)<sup>18</sup> studied hydrofoils with swept leading edges and their experiments showed that the re-entrant jet velocity has a spanwise component if the closure line of the cavity is inclined. The numerical simulation of Schnerr *et al.* (2008)<sup>19</sup> on a twisted hydrofoil showed that the interactions between the re-entrant jet and the spanwise velocity component also cause separation of sheet cavities. The spanwise pressure gradients greatly affect the three-dimensional structure of the cavity, which cause the U-shaped feature observed and discussed by many authors.<sup>20,21</sup> Recently, experimental observations on hydrofoils highlighted the important role played by the two side-entrant jets

which propagated diagonally upstream to the leading edge affecting the attached part of the cavity.<sup>22,23</sup> Such comments were also reported in the numerical study of Long *et al.* (2018)<sup>24</sup> on a twisted hydrofoil using a Lagrangian method.

Another discussion on three-dimensional cavity structures concerns the existence of an oblique mode of the pocket oscillations. This mode was first discussed by Decaix and Goncalves (2013)<sup>25</sup> on a quasi-stable cavity appearing on a Venturi geometry using scale-adaptive simulation (SAS). Later, Timoshevskiy *et al.* (2016)<sup>26</sup> maintained that the oblique mode associated with the development of the spanwise instability exists for all test objects independent of their shape. Yet, the existing visualizations did not clearly report such alternating sheet movement. On the other hand, various experimental studies showed different cavity shedding appearances and behaviors due to the influence of the scale of the geometry and the surface effects.<sup>27,28</sup> Authors observed that at a certain ratio between the length of the sheet cavity and the channel width, an irregular break-off pattern occurred.

The experimental study of complex three-dimensional sheet and cloud cavitation still suffers from the limitation in experimental technique; thus, the numerical simulation appears to be an attractive tool for a better understanding of the two-phase structures and their dynamics. The framework for such turbulent cavitating flows is usually the one-fluid mixture approach based on an average statistical treatment with local thermodynamics assumption. Two main families are often used: the homogeneous equilibrium model (HEM) with a suitable equation of state (EOS) for the liquid–vapor mixture<sup>29–31</sup> or the transport equation model (TEM) or homogeneous relaxation model (HRM) involving a transport equation for the void ratio.<sup>32–35</sup> This equation includes a source term modeling the mass transfer between phases. Another crucial point for cavitating flow simulation is the turbulence modeling. Different approaches have been investigated in order to capture the finer-scale dynamics. First, computations were performed solving the unsteady Reynolds-averaged Navier–Stokes (URANS) equations naturally adapted to the two-phase averaged models<sup>36,37</sup> and more recently using advanced models, such as, SAS,<sup>38,39</sup> filter-based turbulence model (FBM)<sup>40</sup> or partially averaged Navier–Stokes (PANS).<sup>41</sup> As the URANS approach did not fully account for the turbulent-cavitation interactions, large eddy simulations were tested on both hydrofoil and Venturi geometries.<sup>42–46</sup> Yet, due to the large Reynolds number of usual applications (greater than  $1 \times 10^6$ ), the necessity to consider the channel with sidewalls, the use of very small time step, and the problem of the statistics convergence for low-frequency periodic phenomenon, the cost of a well-resolved simulation remains prohibitive even using supercomputers. To circumvent such difficulties, micro-channel cavitating flows has been considered by Egerer *et al.* (2014).<sup>47</sup>

The present study focuses on a 3D quasi-stable cavity flow on a  $4^\circ$  divergent angle Venturi geometry, used in the experiment of Barre *et al.* (2009).<sup>48</sup> The selection of the configuration is motivated by the modest number of experiments with quantitative data and by a configuration compatible with URANS approach. Particular attention is paid to sidewall effects and the 3D topology of the pocket. In the first part, the system of equations and the numerical formulation is developed. Numerical simulations are performed, in a second part, to compare the results with the experimental data. Then, the results of 3D computations with sidewalls and with periodic boundary conditions

are investigated. Numerical tools, such as, power spectral densities (PSD) or spectral proper orthogonal decompositions (SPOD) are used to compare both cases and analyze the flow dynamics. In the last part, the authors’ interpretation of the encountered phenomenon is discussed regarding the dominant mechanisms of sheet cavitation flows.

## II. GOVERNING EQUATIONS

### A. The 1-fluid homogeneous approach

There are several ways to simulate two-phase flows; the most straightforward one is to use a two-fluid model. Nevertheless, in the case of sheet cavitation simulation, this choice would lead to unaffordable computational costs and difficulties related to the interface tracking with the creation and the destruction of vapor pockets or the transfer terms computation due to the phase change. Therefore, a one-fluid homogeneous approach is selected in the present study and hypothesis over thermodynamical and mechanical equilibrium between the liquid and vapor phases are applied.<sup>49</sup> The flow is considered as a mixture and the phases are assumed to share the same pressure, velocity, and temperature. The averaged fraction of presence  $\alpha_k$ , for a given  $k$  phase, is introduced to define the conservative form of mixture properties as

$$\rho_m = \sum_k \alpha_k \rho_k, \quad (1)$$

$$\rho_m u_{i,m} = \sum_k \alpha_k \rho_k u_{i,k}, \quad (2)$$

$$\rho_m e_m = \sum_k \alpha_k \rho_k e_k. \quad (3)$$

### B. The compressible RANS equations

The compressible Reynolds-averaged Navier–Stokes (RANS) system of equations is used to calculate the two-phase flow in the present work. The  $k - \ell$  two-equations model of Smith<sup>50,51</sup> is selected to calculate turbulence quantities. The choice of the turbulence model is motivated by previous works over a panel of models.<sup>15,52,53</sup>

A limiter term is applied to the calculation of the turbulent viscosity property of mixture fluid,  $\mu_{tm}$ . The correction is motivated by previous results,<sup>54,55</sup> which indicate an overestimation of such a quantity for the two-phase flow configurations of interest. The limitation, for the  $k_m - \ell_m$  model, is computed using a function over  $\rho_m$  and is here written as

$$\mu_{tm} = f(\rho_m) \frac{\Phi \sqrt{2k_m \ell_m}}{B_1^{1/3}}, \quad (4)$$

$$f(\rho_m) = \rho_v + \left( \frac{\rho_v - \rho_m}{\rho_v - \rho_l} \right)^n (\rho_l - \rho_v), \quad (5)$$

where  $\rho_v$  and  $\rho_l$  stand for the saturation vapor and liquid density, respectively.  $\Phi$  and  $B_1$  come from the  $k - \ell$  model described by Smith (1994).<sup>51</sup> The limitation is controlled by the parameter  $n \gg 1$  which is precised in Sec. IV. Furthermore, the work of Dandois (2014)<sup>56</sup> indicates the possibility of nonphysical flow results related to an overestimation of the turbulent viscosity in corners. Hence, the quadratic constitutive relation (QCR) correction<sup>57</sup> is applied into the Reynolds stress tensor,

$$\tau_{m,ij}^{\text{QCR}} = \tau_{m,ij} - c_{n11}(O_{ik}\tau_{m,jk} + O_{jk}\tau_{m,ik}), \quad (6)$$

where  $c_{n11} = 0.3$  is an empirical constant and  $O_{ik}$  is the normalized rotation tensor,

$$O_{ik} = \frac{\frac{\partial u_i}{\partial x_k} - \frac{\partial u_k}{\partial x_i}}{\sqrt{\frac{\partial u_n}{\partial x_p} \frac{\partial u_p}{\partial x_n}}}. \quad (7)$$

The mixture viscous stress tensor  $\sigma_m$  and the heat flux vector  $q_m$  are defined as

$$\sigma_{m,ij} = \mu_m \left[ \frac{\partial u_{m,i}}{\partial x_j} + \frac{\partial u_{m,j}}{\partial x_i} - \frac{2}{3} \frac{\partial u_{m,n}}{\partial x_n} \delta_{ij} \right], \quad q_{m,i} = \lambda_m \frac{\partial T_m}{\partial x_i}, \quad (8)$$

where  $\lambda_m = \sum_k \alpha_k \lambda_k$  is the thermal conductivity of the mixture and  $\lambda_k$  is the thermal conductivity of the  $k$ -th phase. Moreover, the mixture turbulent stress tensor  $\tau_m$  and the turbulent heat flux vector  $q_m^t$  are formulated using the Boussinesq relation and the Fourier law, respectively, defined as

$$\tau_{m,ij} = \mu_{tm} \left[ \frac{\partial u_{m,i}}{\partial x_j} + \frac{\partial u_{m,j}}{\partial x_i} - \frac{2}{3} \frac{\partial u_{m,n}}{\partial x_n} \delta_{ij} \right] - \frac{2}{3} \rho_m k_m \delta_{ij}, \quad (9)$$

$$q_{m,j}^t = \lambda_{tm} \frac{\partial T_m}{\partial x_j} \approx \frac{\mu_{tm} C_{pm}}{Pr_t} \frac{\partial T_m}{\partial x_j}, \quad (10)$$

with turbulent Prandtl number  $Pr_t = 1$ . Due to the lack of data over turbulent two-phase flow, the value of the Prandtl number is transposed from aerodynamic studies for monophasic flow. The thermal capacity of the mixture  $C_{pm}$  is defined based on  $C_{pv}$  and  $C_{pl}$ , which stand for the thermal capacity of the vapor and the liquid, respectively,

$$\rho_m C_{pm}(\alpha) = \alpha \rho_v C_{pv} + (1 - \alpha) \rho_l C_{pl}. \quad (11)$$

### C. The four-equation cavitation model

The cavitation modeling approach used in the current work combines the mass conservation, momentum, and energy equations of the Navier–Stokes formulation to another transport equation over the fraction of presence of phases. Moreover, an appropriate set of equations of state is used to model the cavitation.

#### 1. Void ratio transport equation

The void ratio  $\alpha$  is defined as the averaged fraction of presence for the vapor phase. A transport equation for the void ratio is added to complete the cavitation model,

$$\frac{\partial \alpha}{\partial t} + u_{m,j} \frac{\partial \alpha}{\partial x_j} = K \frac{\partial u_{m,j}}{\partial x_j} + \frac{\dot{m}}{\rho_l}. \quad (12)$$

The formulation of the transport equation is based on the work of Saurel *et al.* (2008)<sup>58</sup> and written by Goncalves (2013)<sup>59</sup> in a four-equation model. The mass flow rate  $\dot{m}$  from liquid to vapor<sup>59</sup> can be written as

$$\dot{m} = \frac{\rho_l \rho_v}{\rho_l - \rho_v} \left( 1 - \frac{c_m^2}{c_{\text{Wallis}}^2} \right) \frac{\partial u_{m,j}}{\partial x_j}. \quad (13)$$

The calculation is based on the Wallis speed of sound  $c_{\text{Wallis}}$  which is expressed as a weighted harmonic mean of each one of the two flow phases speed of the sound,<sup>60</sup>

$$\frac{1}{\rho_m c_{\text{Wallis}}^2} = \frac{\alpha}{\rho_v c_v^2} + \frac{(1 - \alpha)}{\rho_l c_l^2}, \quad (14)$$

where  $c_k$  stands for the pure phase speed of sound. The interface density  $\rho_l$  and the constant  $K$  are, respectively, defined as

$$\rho_l = \frac{\rho_l c_l^2 + \rho_v c_v^2}{\frac{c_l^2}{1 - \alpha} + \frac{c_v^2}{\alpha}} \quad \text{and} \quad K = \frac{\rho_l c_l^2 - \rho_v c_v^2}{\frac{\rho_v c_v^2}{\alpha} + \frac{\rho_l c_l^2}{1 - \alpha}}. \quad (15)$$

#### 2. Equations of state

Two different equations of state (EOS) are used for the mixture temperature  $T_m$  and the mixture pressure  $p_m$  depending on a pressure threshold. Pressure and temperature are defined by the stiffened gas EOS for the pure phase while sinusoidal EOS are applied for computing the mixture part of the flow.<sup>53</sup> The threshold is calculated from the vaporization pressure  $P^{vap}$  and a delta pressure based on a chosen parameter  $c_{\text{min}}$  the minimal speed of sound in the mixture,

$$\Delta p_m = \left( \frac{\rho_l - \rho_v}{2} \right) c_{\text{min}}^2 \frac{\pi}{2}. \quad (16)$$

The selection of  $c_{\text{min}}$  is based on the study of Charriere (2015)<sup>61</sup> and set to  $0.472 \text{ m s}^{-1}$ . This parameter allows the activation in advance of the phase change in order to smooth the density gradient around the interface. The density jump between the liquid and the vapor is stiff for a mixture problem. Thus, the mixture pressure is computed according to the relation

$$\begin{cases} p_{SG} & \text{if } p_m \geq P^{vap} + \Delta p, \\ p_{\text{sinus}} & \text{otherwise,} \end{cases} \quad (17)$$

with  $p_{SG}$  and  $p_{\text{sinus}}$  the pressure, respectively, defined by the stiffened gas EOS and the sinusoidal EOS,

$$p_{SG}(\rho_m, e_m) = (\gamma_m - 1) \rho_k (e_m - \hat{q}_m) - \gamma_m p_{m,\infty}, \quad (18)$$

$$p_{\text{sinus}}(\alpha) = P_{vap} + \left( \frac{\rho_l - \rho_v}{2} \right) c_{\text{min}}^2 \arcsin(1 - 2\alpha), \quad (19)$$

where the mixture energy of formation  $\rho_m \hat{q}_m = \alpha \rho_v \hat{q}_v + (1 - \alpha) \rho_l \hat{q}_l$  is calculated from  $\hat{q}_v$  and  $\hat{q}_l$ , which stand, respectively, to the vapor and the liquid energies of formation. The mixture temperature is set equally above and below the pressure threshold,

$$T_m(\rho_m, e_m) = \frac{h_m(\alpha) - \hat{q}_m(\alpha)}{C_{pm}(\alpha)} = \frac{e_m(\alpha) + p_m(\alpha) / \rho_m(\alpha) - \hat{q}_m(\alpha)}{C_{pm}(\alpha)}, \quad (20)$$

where  $h_m$  and  $e_m$  are the specific mixture enthalpy and internal energy, respectively. The mixture speed of sound  $c_m$  is processed following the same approach. Above the pressure threshold, the Wallis speed of sound, Eq. (14), is considered while below the threshold, the speed of sound is computed using the sinusoidal EOS, Eq. (21). The reader can

find more details on the study of the speed of sound development performed by Charriere (2015).<sup>61</sup> For the current case, the phase change does not affect the temperature of the mixture. Therefore, the phase enthalpy  $h_k$  and phase density  $\rho_k$  are defined as constants for a reference temperature  $T_{ref}$ .

$$c_m^2 = (\gamma_m - 1) \frac{\rho_v \rho_l (h_v^{ref} - h_l^{ref})}{\rho_m (\rho_l - \rho_v)} + \frac{Ac_{min}^2}{\sqrt{1 - (A(1 - 2\alpha))^2}}. \quad (21)$$

The phase enthalpy is  $h_k^{ref} = C_{p_k} T_{ref} + q_k$ . The  $A$  coefficient is added in order to guarantee the velocity fitting with Wallis speed of sound above the pressure threshold. In the current case,  $A$  is fixed to 0.9999.<sup>62</sup>

### III. NUMERICAL FORMULATION

The global system is the four-equation model coupled with the turbulence model,

$$\frac{\partial \mathbf{w}}{\partial t} + \nabla \cdot [\mathbf{F}_c(\mathbf{w}) - \mathbf{F}_v(\mathbf{w})] = \mathbf{S}(\mathbf{w}), \quad (22)$$

with

$$\mathbf{w} = \begin{pmatrix} \rho_m \\ \rho_m u_{m,i} \\ \rho_m E_m \\ \alpha \\ \rho_m \psi_k \end{pmatrix}, \quad \mathbf{F}_v = \begin{pmatrix} 0 \\ \sigma_{m,ij} + \tau_{m,ij} \\ (\sigma_{m,ij} + \tau_{m,ij}) u_{m,j} - q_{m,j} - q_{m,j}^t \\ 0 \\ \left( \mu_m + \frac{\mu_m^t}{\sigma_{\psi_k}} \right) \frac{\partial \psi_k}{\partial x_j} \end{pmatrix},$$

$$\mathbf{F}_c = \begin{pmatrix} \rho_m u_{m,j} \\ \rho_m u_{m,i} u_{m,j} + p_m \\ \rho_m E_m + p_m \\ \alpha u_{m,j} \\ \rho_m \psi_k u_{m,j} \end{pmatrix}, \quad \mathbf{S} = \begin{pmatrix} 0 \\ 0 \\ 0 \\ (K + \alpha) \frac{\partial u_{m,j}}{\partial x_j} + \frac{\dot{m}}{\rho_l} \\ C_{\psi_k} \end{pmatrix}.$$

The variable  $\psi_k$  depends on the choice of the turbulence model of  $k$  equations. The turbulent source terms  $C_{\psi_k}$  and the constant  $\sigma_{\psi_k}$  also rely on this model.

#### A. Low Mach number preconditioning

Some parts of the flow into the venturi configuration are supposed to be incompressible (Mach number around 0.1) despite using a compressible hypothesis. Therefore, it is necessary to use a low Mach number preconditioning method to deal with numerical errors and stiffness of the equation system. A preconditioning matrix is computed based on the work of Turkel (1987)<sup>63</sup> using a  $\beta$  all-speed flow parameter proportional to the Mach number,<sup>64</sup>

$$\beta^2 = \min [\max(M^2, \theta M_\infty^2), 1], \quad (23)$$

with the constant  $\theta$  set to 3. The preconditioning is applied only on the dissipation terms to preserve the time discretization consistency.

#### B. Time integration

An explicit third-order strong stability preserving Runge-Kutta method (SSPRK3), described by Spiteri and Ruuth (2002)<sup>65</sup> and Gottlieb (2005),<sup>66</sup> is used as a time-marching scheme. The explicit equation is given by

$$\mathbf{w}^{n+1} = \mathbf{w}^n + h \left( \frac{1}{6} \mathbf{k}_1 + \frac{1}{6} \mathbf{k}_2 + \frac{2}{3} \mathbf{k}_3 \right), \quad (24)$$

with

$$\begin{cases} \mathbf{k}_1 = \mathbf{F}(t_n, \mathbf{w}_n), \\ \mathbf{k}_2 = \mathbf{F}(t_n + h, \mathbf{w}_n + h \mathbf{k}_1), \\ \mathbf{k}_3 = \mathbf{F}(t_n + \frac{h}{2}, \mathbf{w}_n + \frac{h}{4} (\mathbf{k}_1 + \mathbf{k}_2)), \end{cases}$$

in which  $h$  is the time step and  $\mathbf{F}$  represents the numerical fluxes and the source terms of Eq. (22).

#### C. Spatial discretization

A cell-centered finite-volume technique is used for the spatial discretization of the RANS equations. The numerical fluxes are calculated using a centered scheme coupled with an artificial dissipative term. The chosen scheme is based on the second-order Jameson-Schmidt-Turkel (JST),<sup>67</sup> and it is extended to the precision of the third order. Furthermore, an additional term is added to the dissipation, with a density sensor  $\eta_i^{(I)}$ , to allow dissipation around the phase interface,

$$\eta_i^{(I)} = \frac{|\rho_{i+1} - 2\rho_i + \rho_{i-1}|}{\rho_{i+1} + 2\rho_i + \rho_{i-1}}. \quad (25)$$

The global scheme formulation is developed in the [Appendix](#).

#### D. Boundary conditions

The venturi-type geometry configuration used in the current article requires the use of wall and inlet/outlet boundary conditions. The former is implemented here using wall-functions regarding a less expensive representation of the boundary layer while the latter is calculated using Euler characteristic equations.

##### 1. Wall function

The boundary condition for a wall is defined by the following wall function:

$$u^+ = y^+, \quad \text{if } y^+ < 11.13, \\ u^+ = \frac{1}{\kappa} \ln y^+ + 5.25, \quad \text{if } y^+ > 11.13, \quad (26)$$

with the Von Karman constant  $\kappa = 0.41$ . This no slip boundary condition combined with the adiabatic hypothesis for walls results in normal derivatives of the void ratio, the density, and the pressure are set to zero at the wall boundary.

##### 2. Inlet and outlet boundaries

The void ratio  $\alpha$ , the phase density  $\rho_k$ , and the velocity components are imposed at the inlet boundary. Then, the pressure is computed using the Euler's characteristic equations,



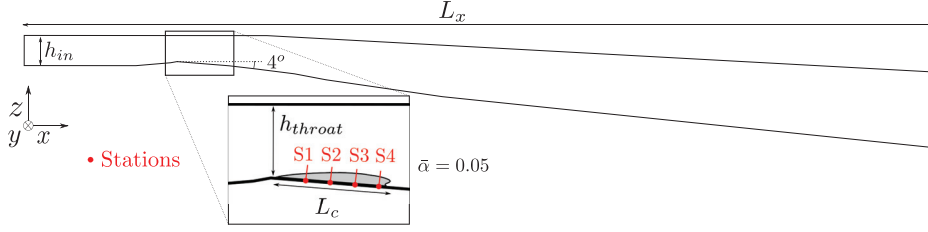


FIG. 1. Schematic view of the venturi used in the computation.

$$\begin{aligned}
 -c^2(\rho^b - \rho^s) + (P^b - P^s) &= 0, \\
 v^b - v^s &= 0, \\
 \rho(\alpha^b - \alpha^s) - K(\rho^b - \rho^s) &= 0, \\
 (\lambda_+ - u)(P^b - P^s) + \rho\beta^2 c^2(u^b - u^s) &= 0, \\
 (\lambda_- - u)(P^b - P^s) + \rho\beta^2 c^2(u^b - u^s) &= 0,
 \end{aligned} \tag{27}$$

where  $b$  index stands for boundary variables and  $s$  index stands for variables computed with the numerical scheme.  $\lambda_{\pm}$  are the highest and the lowest eigenvalues of the preconditioning system. The static pressure is selected while other variables are calculated using the characteristic equations at the outlet boundary condition.

#### IV. VENTURI CONFIGURATION AND COMPARISON

The present section is devoted to introduce the studied case and to compare the numerical results with experimental data. Previous computations and comparisons with literature using the current cavitation model, for different configurations (expansion tube, underwater explosion with cavitation, compression of a vapor bubble, venturis, shock tubes, ...), have already been published.<sup>53,59,68,69</sup>

##### A. Case setup

A  $4^\circ$  divergence angle venturi configuration, as the one used in the experiment of Barre *et al.* (2009),<sup>48</sup> is selected for the study. Figure 1 illustrates the venturi geometry, and Table I indicates flow and sections parameters used in the current case. Probes positioning is calibrated to capture data adjacent to the cavitation pocket at four stations (S1–S4 in Fig. 1) located at 20.9, 38.4, 55.8, and 73.9 mm from the venturi throat. The inflow parameters are set as followed: the streamwise velocity  $u_{in} = 10.8 \text{ m s}^{-1}$ , the temperature  $T_{in} = 293 \text{ K}$ , the void ratio  $\alpha_{in} = 10^{-10}$ , the density  $\rho_{in} = 1000.831 \text{ kg m}^{-3}$ , and the vaporization pressure  $P_{vap} = 2339 \text{ Pa}$ . The inflow cavitation number  $\sigma_{in}$  is 0.55 and the inflow Reynolds number is  $Re_{in} = \rho_{in} u_{in} h_{in} / \mu_{in} = 5.4 \times 10^5$ . The outflow pressure is calibrated to correspond with this cavitation number. The study is focused on one operating point corresponding to the selected experimental setup.

Calculations over the  $4^\circ$  divergent angle venturi apply 2D and 3D computational domains with  $340 \times 72$  and  $340 \times 72 \times 72$  mesh cells represented in Fig. 2, respectively. The grids are designed in a structured fashion concerning maximum normal distance to the walls

TABLE I. Geometric dimensions.

$L_x$	$h_{in}$	$h_{throat}$	$L_y$
1.512 m	0.05 m	0.0437 m	0.044 m

of wall-bounded cells,  $z^+$  according to Fig. 1 coordinates, between 10 and 15 in the area of interest. The  $n$  parameter of the Reboud limiter, from Eq. (5), is set to 10 in the 2D calculation<sup>52</sup> and 19 in the 3D calculation. As observed in other works,<sup>70–72</sup> the choice of  $n$  in the 3D configuration is motivated by an under-prediction of the re-entrant jet development for the k-1 model using  $n=10$ . For that reason, the  $n$  parameter is calibrated to correctly capture the re-entrant jet by comparing with experimental data. The dissipative terms parameters of the extended Jameson–Schmidt–Turkel scheme  $k_2$ ,  $k_2^I$ , and  $k_4$  are, respectively, set to 1.0, 1.5, and 0.045. Furthermore, the time step is fixed to  $4.58 \times 10^{-6}$  and  $2.29 \times 10^{-7}$  s for the 2D and 3D simulations, respectively, and a total of 2.06 s physical time is run for the two numerical studies. Table II presents the required parameters for the computation of the cavitation model for both phases. Another 3D computation is carried out on the same geometry with the same parameters except for a twice larger width and periodic side boundary conditions.

##### B. Comparison with experimental data

The numerical results of the in-flow simulation are then compared to the experimental data from Barre *et al.* (2009).<sup>48</sup> This experiment provides measures of time-averaged velocity, void ratio, and wall pressure profiles at stations located in the midspan of the venturi.

##### 1. Velocity and void ratio profiles

Profiles of time-averaged velocity and time-averaged void ratio from 2D and both 3D simulation results are compared with experimental data at different positions in Figs. 3 and 4. Numerical results have similar behavior for the first station S1. The capture of the re-entrant jet is in a good match with the experiment for the numerical results, apart from the 3D periodic case at S2, since the negative values of the velocity are correctly determined, as observed in the velocity profiles at the three other stations (S2, S3, and S4). The void ratio profiles are in good accordance for all computations but are in better agreement for the 3D case with sidewalls, whose results indicate a better representation of the pocket size and shape when compared to the 2D and 3D periodic calculations. The 3D computation with sidewalls correctly captures the physical behavior of the cavitating flow. Moreover, the time-averaged results of this case are sensibly conformed with the experimental results. Differences between 3D computations with sidewalls and periodic boundary conditions are discussed later in the paper.

##### 2. Wall pressure profiles

The mean wall pressure and pressure fluctuations profiles are extracted from computations and are presented in Fig. 5 in

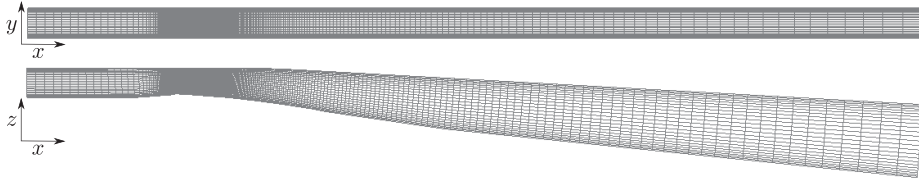


FIG. 2. Mesh generation of the 3D case represented with one visible mesh point out of three in the  $y$  and  $z$  directions.

TABLE II. Parameters of the cavitation model.

	$\rho^{sat}$ (kg/m <sup>3</sup> )	$\Gamma$	$p_{\infty}$ (Pa)	$q$ (J/kg)	$Cp$ (J/K kg)
Liquid	998.16	1.01	$1.211 \times 10^7$	$-1.142 \times 10^6$	4183
Vapor	0.0173	1.32	0	$1.985 \times 10^6$	1883

comparison with experimental data. The wall pressure profile from the 2D and 3D calculations is in good agreement with experimental data along the cavity and reasonably fits the experimental data downstream the cavity. Nevertheless, the root mean square (RMS) fluctuations are slightly underestimated for all cases. Moreover, oscillations detected in the 2D computation are not observed in 3D computations.

## V. GLOBAL BEHAVIOR

The current section is dedicated to the first interpretation of numerical results from computations over 3D configurations with and without sidewalls. A statistical analysis of the calculation data is performed to investigate the time-averaged and dynamical global behavior of such flow configuration. Data are extracted at a  $2.3 \times 10^{-3}$  s time step.

### A. Time-averaged data analysis

According to the experimental observations of the Venturi,<sup>48</sup> a weakly fluctuating cavity emerges without any large vapor shedding process. A time-averaged cavity length  $L_c$  between 70 and 85 mm, estimated with an  $\alpha$  contour of 0.05, is observed in the experiment. Numerical results for the case with sidewalls present a pocket length of

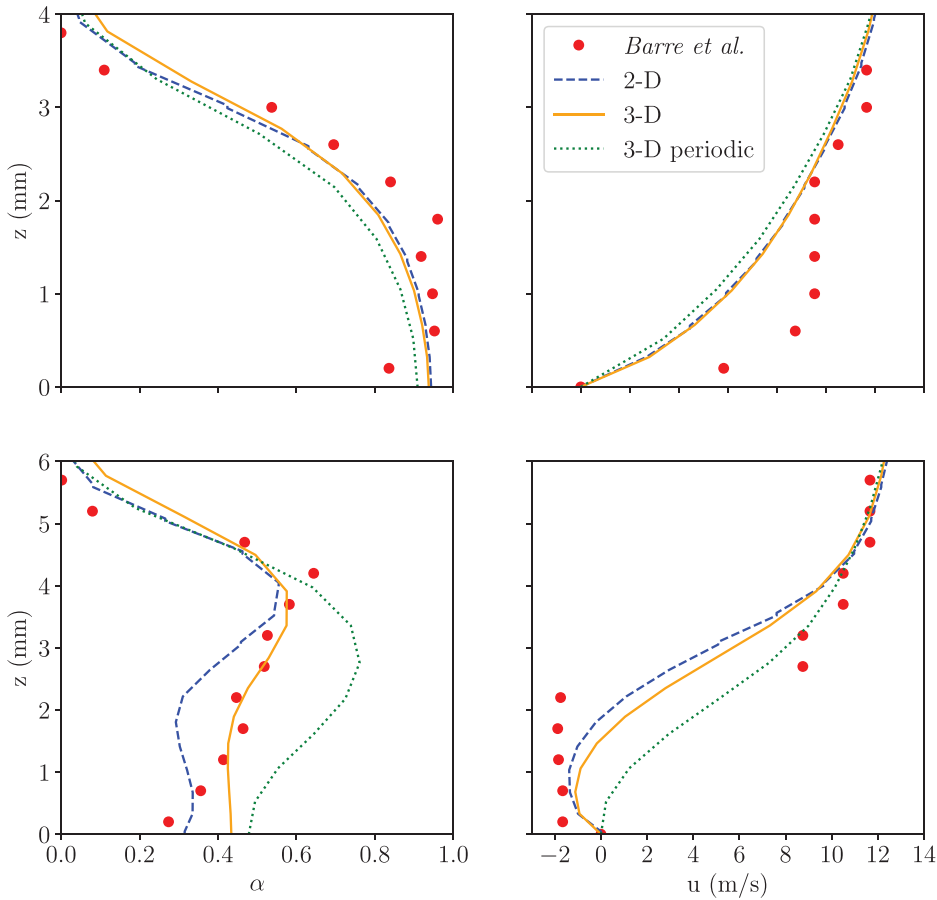


FIG. 3. Time-averaged comparison at midspan between experiment, 2D, 3D, and 3D periodic for void ratio (left) and velocity (right) at stations S1 (top) and S2 (bottom).

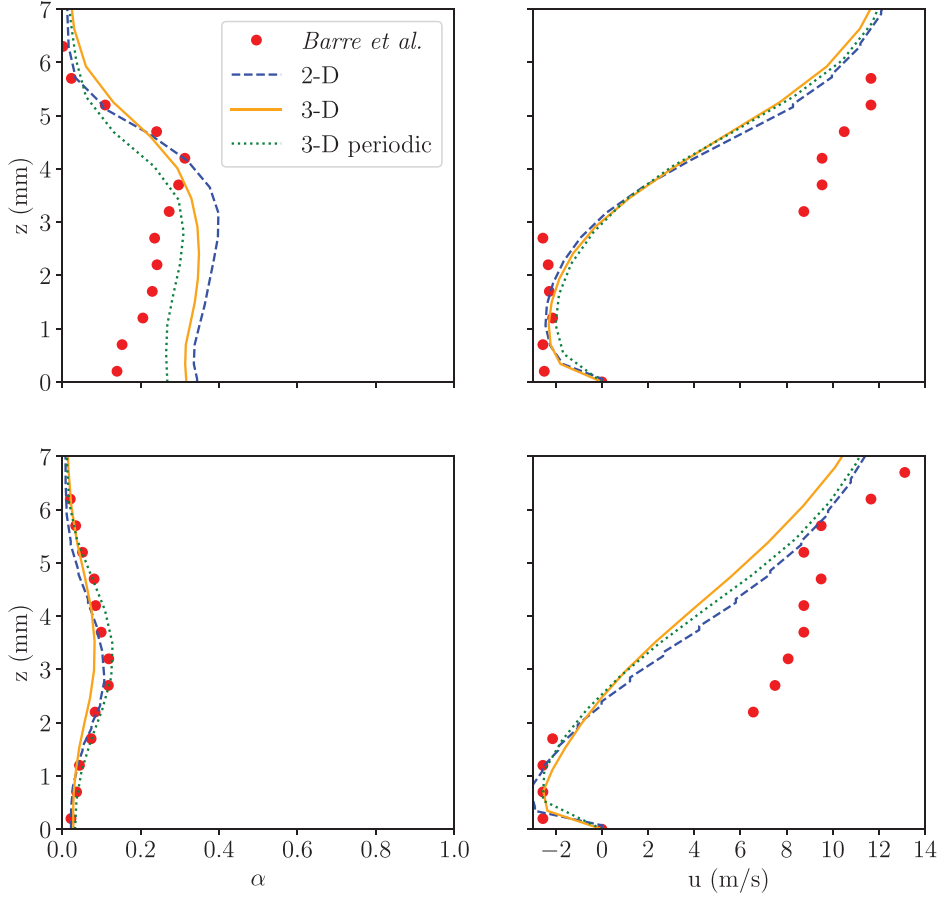


FIG. 4. Time-averaged comparison at midspan between experiment, 2D, 3D, and 3D periodic for void ratio (left) and velocity (right) at stations S3 (top) and S4 (bottom).

$L_c = 78.8$  mm, which is consistent with the experiment. This length is selected to be the characteristic length for the current study. The maximum value of the time-averaged re-entrant jet velocity is also used as the characteristic velocity,  $u_{\max}^{\text{jet}} = 2.38$  m s<sup>-1</sup>. The selection of these two characteristic variables is motivated by the observation of the cavitating flow behavior and the identification of the leading mechanism. Moreover, the study of Dular and Bachert (2009)<sup>73</sup> defines the re-entrant jet velocity at the cavity closure and the length of the attached vapor pocket as the most correct values to investigate the cavitating flow over a hydrofoil. The maximum reverse flow is also considered as the characteristic velocity in noncavitating flows with separation bubble; Hammond and Redekopp (1998)<sup>74</sup> and Rist and Maucher (2002)<sup>75</sup> show the important role of the reverse flow in the triggering of instabilities. The Strouhal number is then defined as

$$St = \frac{L_c f}{u_{\max}^{\text{jet}}}. \quad (28)$$

In the literature, for sheet to cloud cavitation cases, the Strouhal number is mostly defined with inlet velocity.<sup>14,76,77</sup> The choice of the characteristic velocity will be justified later in the paper by investigating the resulting Strouhal number. Variables with a superscript \* in the manuscript are dimensionless and are calculated using the characteristic length  $L_c$  and characteristic velocity  $u_{\max}^{\text{jet}}$ .

A symmetrical attached cavity is detected in Fig. 6(a) with a longer cavitation pocket length near sidewalls than near of the midplane of the Venturi. The U-shape of the cavitation pocket is detected as described in many Refs. 20 and 21. The lower amount of void ratio suggests vapor release and/or pocket oscillations around the midwidth. Figure 6(b) presents the cavitation pocket shape for the periodic case. Unlike the case with sidewalls, the cavity length is constant in all the venturi width. Then, the observation of the flow direction velocity in Figs. 7(a) and 7(b) underlines the presence of the re-entrant jet along the wall. The jet geometry is symmetric and is not present close to sidewalls whereas it is localized in all the venturi width for the periodic case. Moreover, for the venturi with sidewalls, the vertical velocity is also symmetric, while the spanwise velocity is antisymmetric.

## B. Dynamic analysis

A study of the flow dynamics is carried out to statistically interpret the behavior of the cavitation pocket and velocity components over time for configurations with sidewalls and with side periodic boundaries. First, the analysis is focused on the case with sidewalls. Figure 8 shows the void ratio  $\alpha$  into the flow at six different times. It is worth to notice that the pocket shape is not symmetric and evolves with time. A small high-frequency vapor shedding appears around the cavity closure while the pocket seems to oscillate in the spanwise



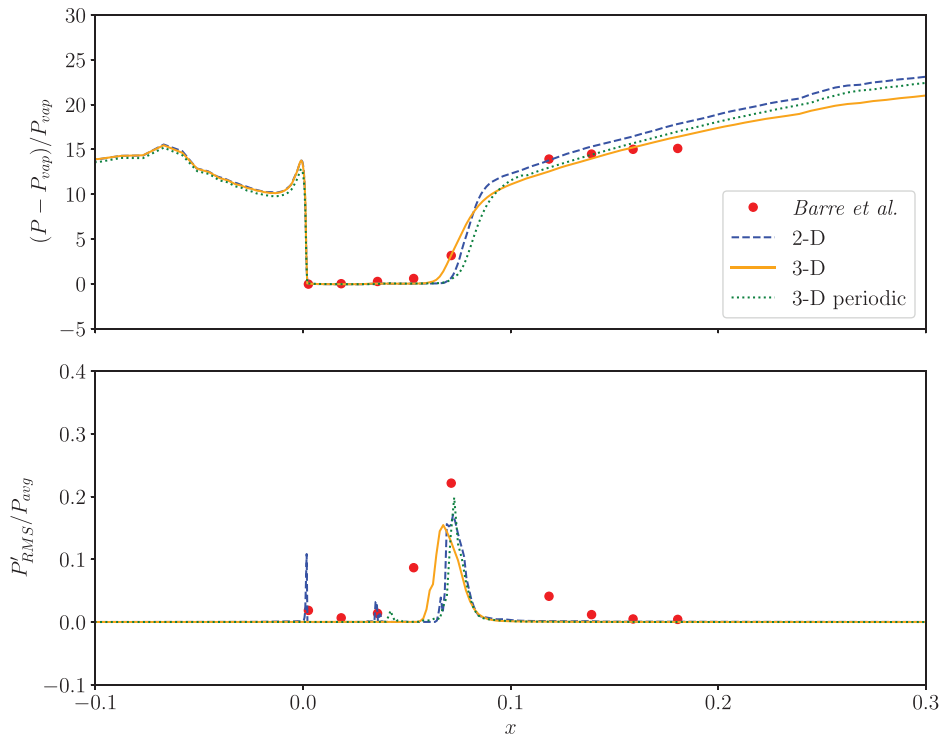


**FIG. 5.** Time-averaged comparison between experiment, 2D, 3D, and 3D periodic for wall pressure and wall pressure RMS over wall pressure.

direction. A statistical analysis is carried out to check any data fluctuations within the venturi flow. The RMS results over the spanwise velocity  $v$  are presented in Fig. 9. The highest values of fluctuation are located at the pocket closure, mostly around the midwidth. Therefore, it corroborates the occurrence of a spanwise oscillation of the flow nearby this area.

Subsequently, the time evolution of flow variables is extracted for points in the flow direction and in the spanwise direction to perform power spectral densities (PSD). The result is presented as a map of PSD along the longitudinal and spanwise axis. PSD maps provide information to identify any high-energy frequencies and locate the associated phenomenon into the venturi. Figure 10 presents the PSD

map over the spanwise direction, respectively, for the void ratio and the spanwise velocity, positioning at almost the two-thirds of the mean cavity length. A sample of signal used for the PSD computations can be observed in Fig. 13. It is worth to remark that no particular dynamics are detected inside the attached cavitation pocket. A dominant Strouhal number of 1.09 is highlighted around the cavity closure by detecting the highest PSD energy values. These are underlined in the midwidth of the venturi for velocity and near sidewalls for the void ratio. Similar behavior is observed for PSD maps downstream the cavity but with the appearance of a low frequency for the void ratio. Regarding previous remarks over snapshots of Fig. 8 and the RMS of the spanwise velocity, the Strouhal number  $St_0 = 1.09$  seems to be

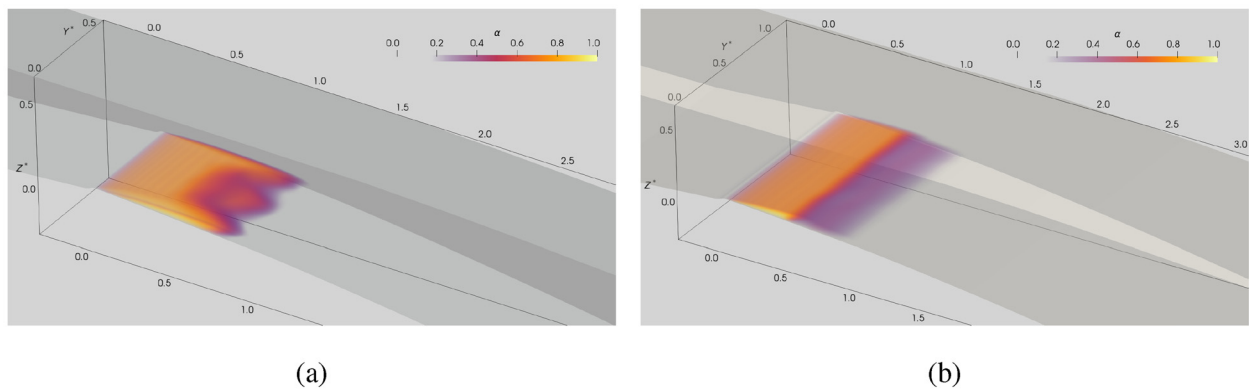
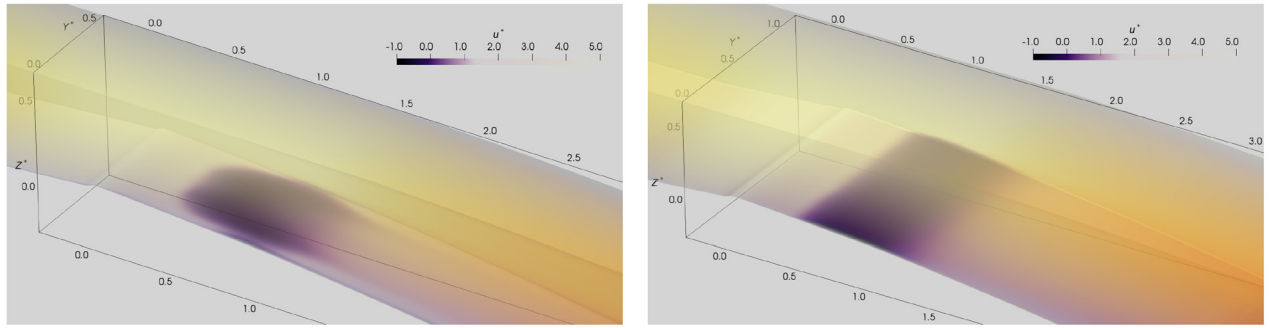


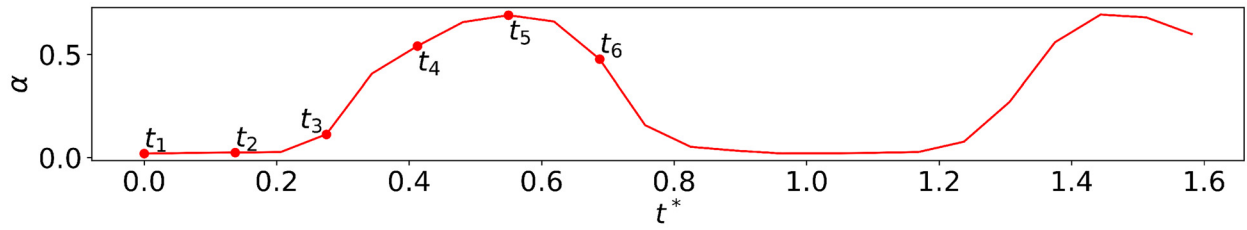
**FIG. 6.** Volume rendering of the time-averaged void ratio: (a) for the venturi with sidewalls and (b) for the venturi with side periodic boundary conditions.



(a)

(b)

FIG. 7. Volume rendering of the time-averaged streamwise velocity: (a) for the venturi with sidewalls; (b) for the venturi with side periodic boundary conditions.



(a) Void ratio signal.

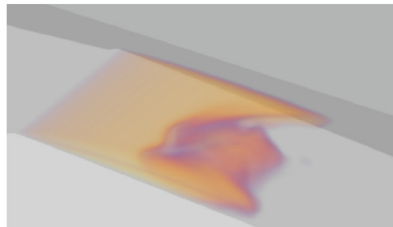
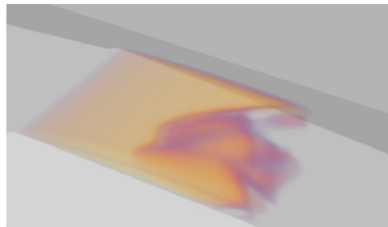
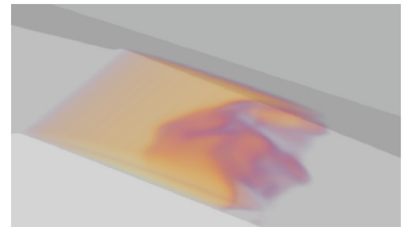
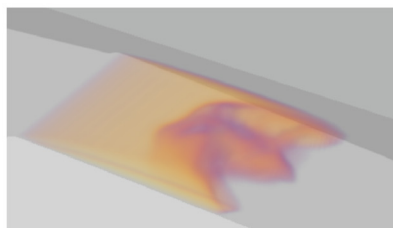
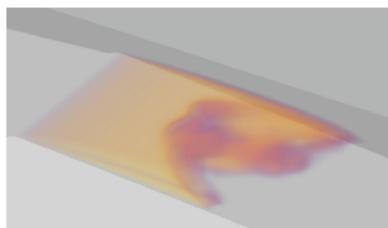
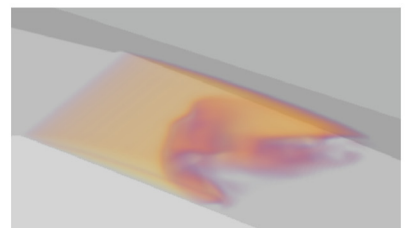
(b)  $t_1$ (c)  $t_2$ (d)  $t_3$ (e)  $t_4$ (f)  $t_5$ (g)  $t_6$ 

FIG. 8. Time evolution of the attached cavity with snapshots separated by  $\Delta t = 4.58 \times 10^{-3}$  s with a volume rendering; (b)–(g) Snapshots extracted at different time represented in the void ratio signal (a).

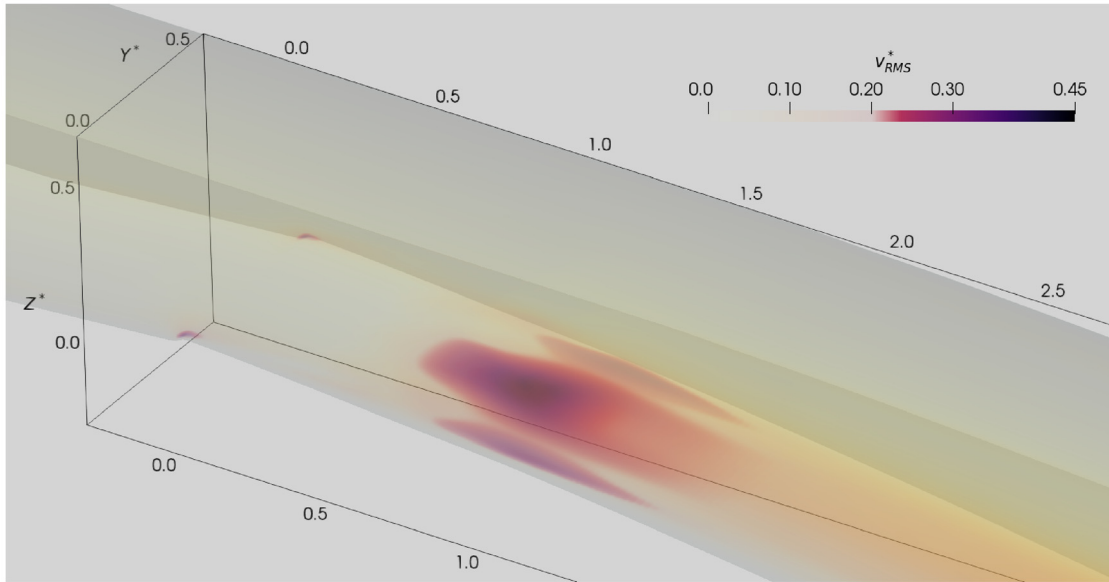


FIG. 9. Volume rendering of the RMS fluctuation of the spanwise velocity  $v$ .

linked to a spanwise oscillation of the cavitation pocket. First harmonics of  $St_0$  also emerge from the PSD map for the void ratio.

Figure 11 shows the PSD map over the streamwise direction for the void ratio at the quarter width. As previously noticed, neither particular dynamic is detected in the midwidth for the void ratio.

Nevertheless, at the quarter width, the highest values of the PSD are observed around the cavity closure at the same Strouhal number  $St_0$ .

Figure 12 presents the PSD map over the streamwise direction for the spanwise velocity, at two positions on the spanwise axis: one located in the midwidth ( $y^* = L_y^*/2$ ) and another one in the eighth

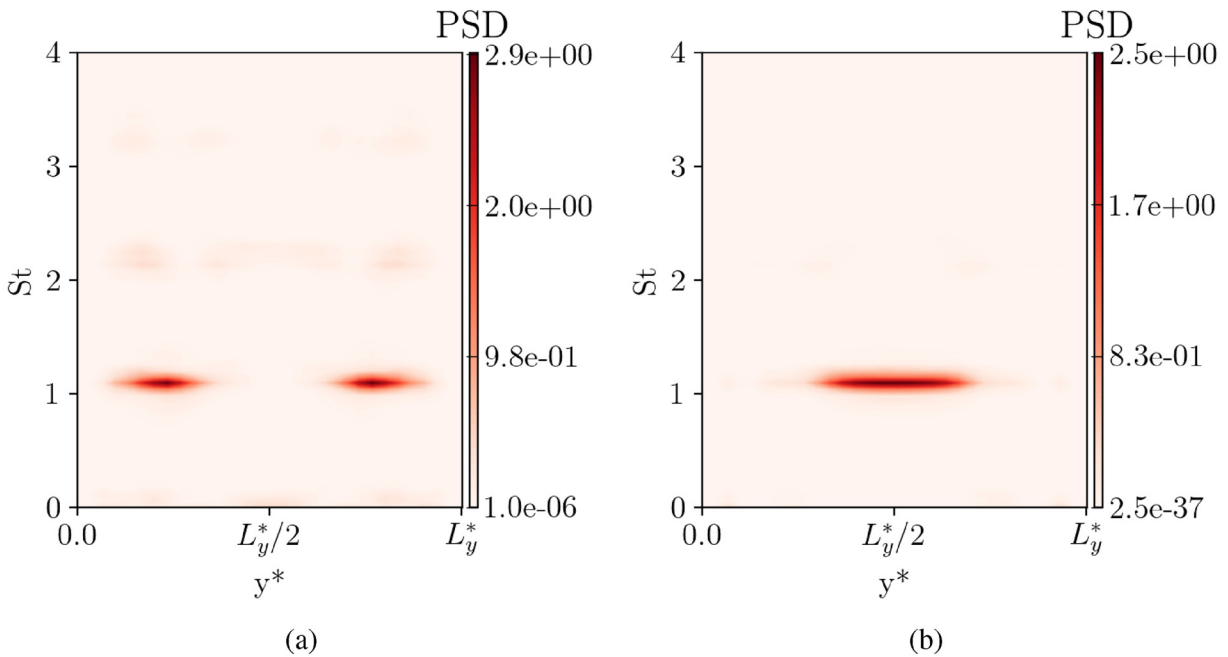
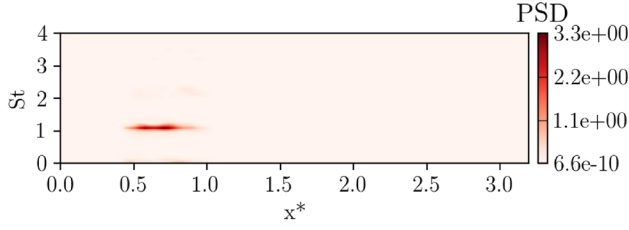


FIG. 10. PSD maps along spanwise axis at  $x^* = 0.64$  and at a vertical distance  $z_p^* = 0.032$  from the bottom wall: (a) for the void ratio  $\alpha$  and (b) for the spanwise velocity  $v$ .



**FIG. 11.** PSD map for  $\alpha$  along longitudinal axis at  $y^* = L_y^*/4$  and at a vertical distance  $z_p^* = 0.032$  from the bottom wall.

width ( $y^* = L_y^*/8$ ). The same behavior as for the void ratio is underlined at both positions but with also a propagation of the dynamics downstream. Furthermore, at the eighth width positioning, the two first harmonics are also detected around the cavity closure and downstream.

The PSD analysis identified a dominant dynamics at the Strouhal number  $St_0$ . This phenomenon appears nearby the cavity closure and is propagated downstream. Furthermore, a motion of the cavitation pocket has been highlighted close to sidewalls. A spanwise velocity variation also emerges at the midwidth of the venturi. The dominant flow fluctuations and its location have been determined. However, a correlation study is carried out by extracting the flow variables over time close to both sidewalls to specify the cavity behavior. One can remark that, in Fig. 13, data are in opposition of phase, which can lead to a conclusion that the cavitation pocket motion is assimilated to a periodic oscillation from one sidewall to another.

Dynamics analysis of the case with periodic boundaries is then carried out to investigate the sidewall effects. First observations of snapshots do not allow to identify any periodic oscillations of the cavitation pocket. However, a three-dimensional dynamic behavior of the cavity is observed around the closure. Figure 14 shows PSD maps along the longitudinal axis for the void ratio and the spanwise velocity component. The same Strouhal number  $St_0$  and its first harmonic are

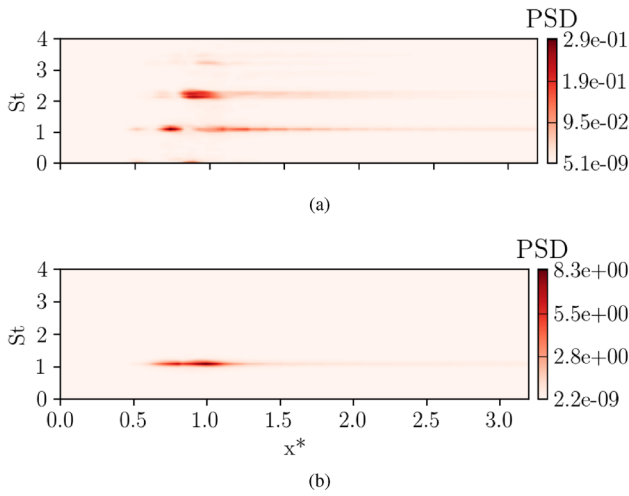


**FIG. 12.** PSD maps for spanwise velocity  $v$  along longitudinal axis at a vertical distance  $z_p^* = 0.032$  from the bottom wall: (a) at  $y^* = L_y^*/8$  and (b) at  $y^* = L_y^*/2$ .

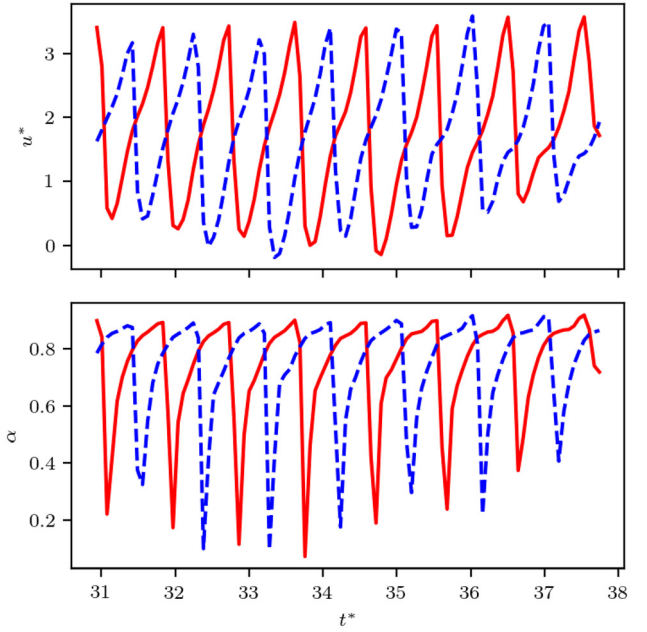


**FIG. 13.** Temporal evolution of the flow direction velocity  $u$  and the void ratio  $\alpha$  at  $x^* = 0.64$  along both sidewalls (one in red, the other in blue) for the case with sidewalls.

extracted around the cavity closure for both variables and propagated downstream for the spanwise velocity component. The same Strouhal number is obtained from PSD maps over the results of the periodic case and the case with sidewalls. Hence, it suggests that the cavitation pocket fluctuations are not dependent of the presence of sidewalls. A deepened analysis is performed in Sec. VII to confirm this observation.

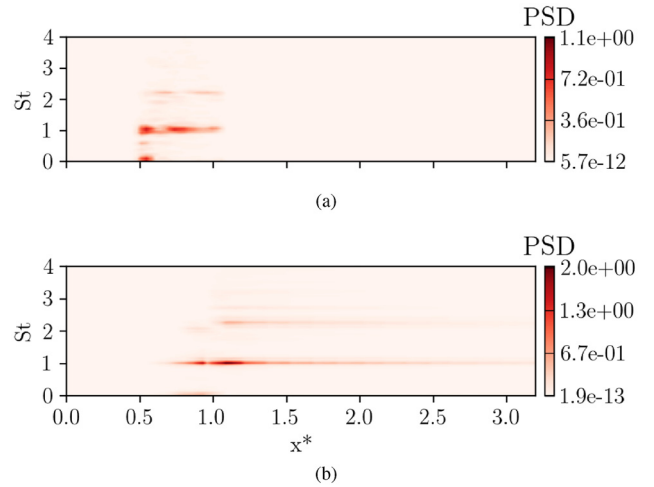


**FIG. 14.** PSD maps of the periodic case along longitudinal axis at the midwidth and at a vertical distance  $z_p^* = 0.032$  from the bottom wall: (a) for the void ratio  $\alpha$ ; (b) for the spanwise velocity  $v$ .

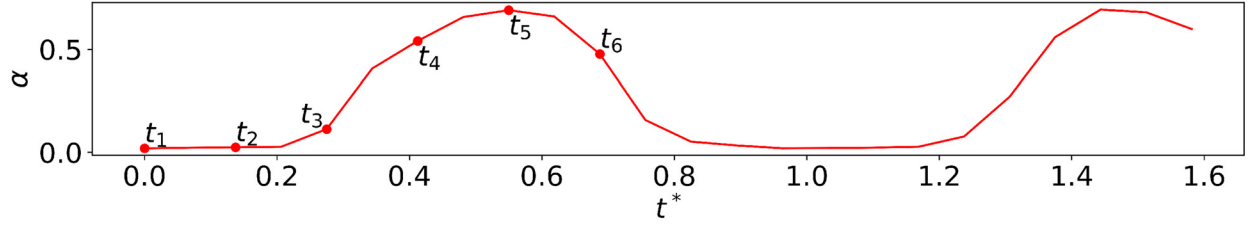
## VI. RE-ENTRANT JET

In this section, the behavior of the re-entrant jet is studied in regard to the cavitation pocket oscillation for the case with sidewalls. Figure 15 describes the re-entrant jet position in relation to the cavity position at different times over an oscillation period. As expected, the re-entrant jet is located nearby the cavity closure and is time-dependent. Moreover, PSD maps of the streamwise velocity highlight a dynamics around the cavity closure based on the Strouhal number  $St_0$ . Thus, the re-entrant jet oscillates at the same frequency as the cavitation pocket from a spanwise wall to another. However, the position of the re-entrant jet compared to the cavity has to be determined. Figure 16 presents the time evolution of the void ratio  $\alpha$  and the flow direction velocity  $u$  around the cavity closure at the quarter width. The negative values of the streamwise velocity component illustrate the re-entrant jet position and the highest value of the void ratio represents the cavity position. The time evolution of  $u$  and  $\alpha$  indicates an opposition in both oscillations of the cavitation pocket and the re-entrant jet.

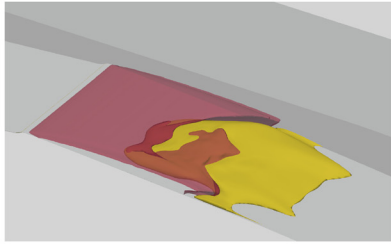
When the pocket is asymmetric in the spanwise direction, the re-entrant jet presents an opposite asymmetry. The cavity growth near side walls is smoother when compared to the cavity disappearance at the same position. For the re-entrant jet signal, it is the opposite behavior, high growth, and a smoother decrease. Therefore, the maximum peaks of void ratio exactly correspond, in time, to the maximum ones of flow direction velocity, while both minimum ones are time-shifted. Hence, the spanwise movement is not uniform. When the cavity moves nearby sidewalls, it is pushed back with acceleration and, at the same time, the re-entrant jet motion changes its spanwise direction with an acceleration. Such behavior indicates a possible causality effect between both phenomena.

## VII. MODAL DECOMPOSITION ANALYSIS

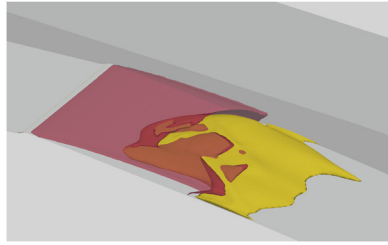
Early results highlighted a dominant flow component at the Strouhal number  $St_0$  probably linked to a cavitation pocket oscillation. Modal decomposition analysis is performed to corroborate previous



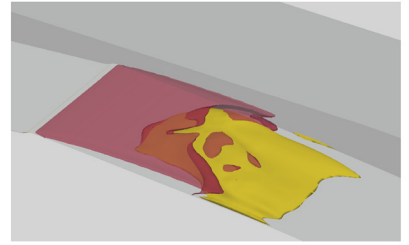
(a)



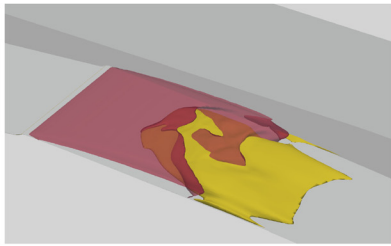
(b)  $t_1$



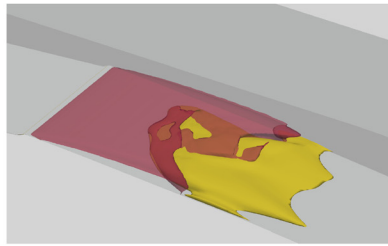
(c)  $t_2$



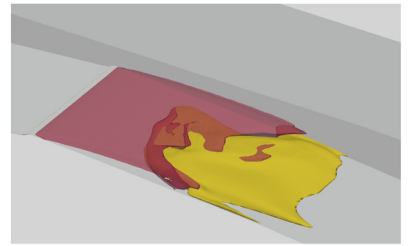
(d)  $t_3$



(e)  $t_4$



(f)  $t_5$



(g)  $t_6$

**FIG. 15.** Dynamics of the re-entrant jet regarding the vapor cavity: (a) void ratio over time at  $x^* = 0.8$  and  $y^* = 3L_y^*/4$  for the case with sidewalls; (a)–(f): Snapshots with time step  $\Delta t = 4.58 \times 10^{-3}$  s of  $\alpha = 0.5$  (purple) and  $u^* = -0.1$  m s $^{-1}$  (yellow) contours.

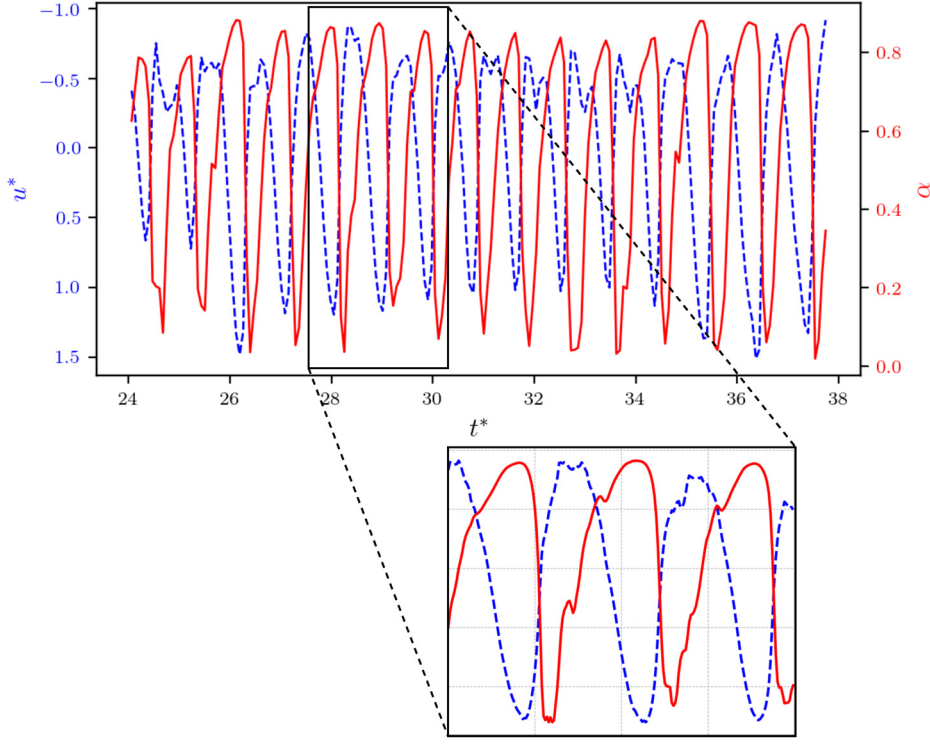


FIG. 16. Time evolution of the flow direction velocity  $u$  and the void ratio  $\alpha$  at  $x^* = 0.64$  and  $y^* = L_y/4$  for the case with sidewalls.

observations. The spectral proper orthogonal decomposition (SPOD) is computed from the computational data to identify spatiotemporal mechanisms. The choice of the SPOD is motivated by the extraction of spatiotemporal modes which is the most coherent method to study unsteady flow as presented by Towne *et al.* (2018).<sup>78</sup> The SPOD methodology employed, based on Schmidt and Colonius (2020)<sup>79</sup> work, is described below.

Given a snapshot  $\mathbf{q}'_i = \mathbf{q}_i - \bar{\mathbf{q}}$  which represents the fluctuation of the flow result for the density and the velocity components at a time  $t_i$ , the data matrix  $\mathbf{Q}$  is defined as

$$\mathbf{Q} = [\mathbf{q}'_1 \mathbf{q}'_2 \mathbf{q}'_3 \dots \mathbf{q}'_N], \quad (29)$$

with  $\bar{\mathbf{q}}$  the temporal mean. The cavitating flow is modeled using a compressible formulation; therefore, the instantaneous energy is defined based on the Chu norm<sup>80</sup> with the temperature fluctuation neglected. It is expressed with a spatial inner product,

$$\|\mathbf{q}'_i\|_E = \langle \mathbf{q}'_i, \mathbf{q}'_i \rangle_E = \mathbf{q}'_i{}^T \mathbf{M} \mathbf{q}'_i = \mathbf{q}'_i{}^T \mathbf{R}^T \mathbf{R} \mathbf{q}'_i = \|\mathbf{R} \mathbf{q}'_i\|_2, \quad (30)$$

$$\mathbf{M} = \mathbf{R}^T \mathbf{R} = \begin{pmatrix} \frac{\bar{T}}{2\bar{\rho}\gamma M_\infty^2} \mathbf{A} & 0 & 0 & 0 \\ 0 & \frac{\bar{\rho}}{2} \mathbf{A} & 0 & 0 \\ 0 & 0 & \frac{\bar{\rho}}{2} \mathbf{A} & 0 \\ 0 & 0 & 0 & \frac{\bar{\rho}}{2} \mathbf{A} \end{pmatrix},$$

where  $\mathbf{A}$  stands for the diagonal cell volume matrix,  $\bar{T}$  the temporal mean temperature,  $\bar{\rho}$  the temporal mean density, and  $M_\infty$  the far-field

Mach number. The first step of the SPOD is to apply Welch's method to the data matrix. It consists of separating the data in  $N_{blk}$  overlapping blocks of snapshots and then performing the discrete Fourier transform on each block. Thus,  $N_{blk}$  matrix of  $N_{freq}$  discrete frequency realizations is obtained. Then, the Fourier realizations of all blocks are grouped by frequency to obtain  $N_{freq}$  matrix  $\hat{\mathbf{Q}}_{fr}$ ,

$$\hat{\mathbf{Q}}_{fr} = [\hat{\mathbf{q}}_{fr}^1 \hat{\mathbf{q}}_{fr}^2 \hat{\mathbf{q}}_{fr}^3 \dots \hat{\mathbf{q}}_{fr}^{N_{blk}}], \quad (31)$$

where  $\hat{\mathbf{q}}_{fr}^i$  denotes the Fourier realization of the  $i^{th}$  block at the frequency  $fr$ . The second part of the SPOD is to compute the cross-spectral density matrix at each frequency,

$$\mathbf{S}_{fr} = \hat{\mathbf{Q}}_{fr} \hat{\mathbf{Q}}_{fr}^*. \quad (32)$$

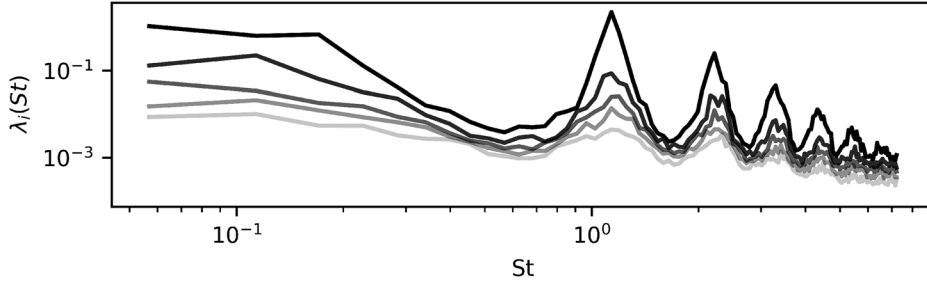
$(\cdot)^*$  denotes the complex conjugate. Thus, the SPOD modes  $\Psi_{fr}$  are generated by the eigenvalue decomposition of the cross-spectral density matrix,

$$\mathbf{S}_{fr} \mathbf{M} \Psi_{fr}^* = \Psi_{fr} \Lambda_{fr}, \quad (33)$$

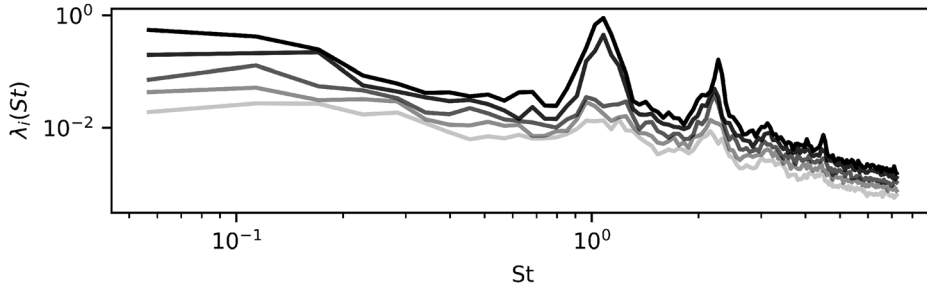
with  $\Lambda_{fr}$  the diagonal matrix of eigenvalues representing the mode energy from the most energetic, corresponding to the leading SPOD mode, to the less one.

Figure 17 presents the SPOD spectrum for both studied cases. The Strouhal number  $St_0 = 1.09$  and its harmonics emerge from the spectrum for the simulation with sidewalls. Similarly, for the periodic side simulation, the Strouhal number  $St_0$  is extracted from the spectrum but with only the first harmonic. Hence, the dominant flow mechanism seems to be characterized by the Strouhal number  $St_0$ .





(a)



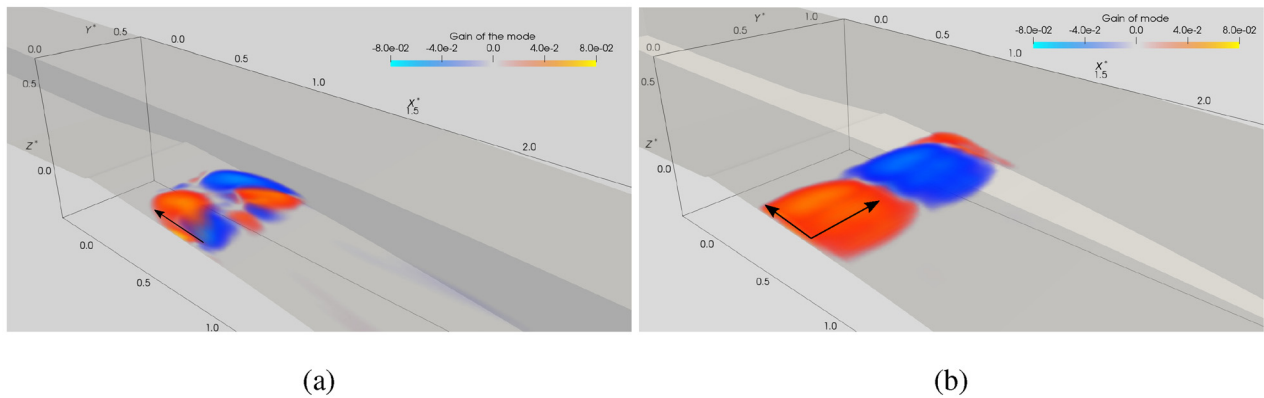
(b)

**FIG. 17.** SPOD spectra representing energy gain over Strouhal number: (a) for the sidewalls case and (b) for the periodic case. The black to gray scale represents the most energetic mode to the less energetic one for each Strouhal number.

Moreover, for the sidewalls case, the observation of the energy gain gap between the first and the second SPOD mode at the corresponding frequency proves that the associated mechanism is mostly led by the first mode. Nevertheless, for the periodic side case, the energy gap is located between the second and the third mode. The associated mechanism is then mostly driven by the two first modes.

Figures 18–21 show the real part of the dominant mode for density and velocity components for both cases. Arrows underline the time evolution of the mode. For the density in the simulation with sidewalls in Fig. 18(a), the mode is antisymmetric and corresponds to a spanwise oscillation coupled with a nonuniform upstream flow. It is

noticed that the midwidth plane is not affected by the fluctuations. Similarly, the spanwise oscillations are observed by the antisymmetric mode for the streamwise velocity in Fig. 19(a) and the vertical velocity in Fig. 21(a) with the upstream behavior. Conversely, the mode of the spanwise velocity in Fig. 20(a) is symmetric but also corresponds to the spanwise oscillation between sidewalls. However, in contrast to the density oscillation, the dominant mode for velocity components is also propagated downstream by the flow with a higher speed. These results substantiate the previous ones observed in the PSD analysis. By examining the harmonic modes, it is determined that, contrary to the dominant one, the first presents a symmetric behavior for density,



(a)

(b)

**FIG. 18.** Volume rendering of the dominant mode of the SPOD for  $\rho$  at  $St = 1.09$ ;  $\rightarrow$ : Time evolution behavior: (a) for the case with sidewalls and (b) for the case with periodic side boundaries.

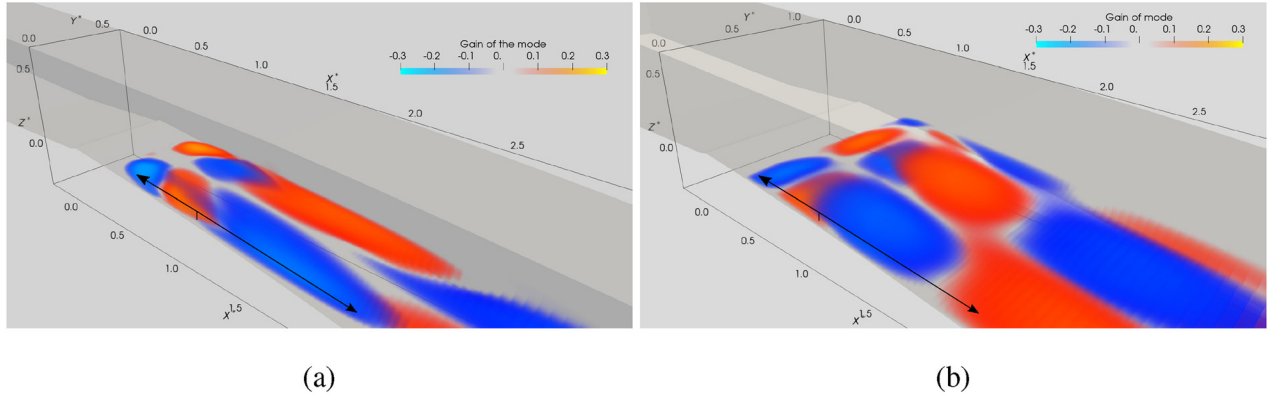


**FIG. 19.** Volume rendering of the dominant mode of the SPOD for  $u$  at  $St = 1.09$ ;  $\rightarrow$ : Time evolution behavior: (a) for the case with sidewalls and (b) for the case with periodic side boundaries.

longitudinal velocity and vertical velocity while it illustrates an anti-symmetric behavior for the spanwise velocity. Nevertheless, the second harmonic mode shows the same symmetrical and antisymmetrical characteristics as the dominant mode. Hence, an alternation of symmetry and antisymmetry is observed in harmonic modes. The dominant SPOD mode for the case with periodic sides mainly differs from the sidewalls case for the density and the spanwise velocity component. In the first one, as observed in Fig. 18(b), a spanwise alternation of the cavitation pocket and an upstream flow are depicted. Then, a nonhomogeneous spanwise motion is also captured around the cavity closure. It has to be noticed that the second SPOD mode, at the Strouhal number  $St_0$ , presents a similar behavior with an opposite direction for the spanwise motion. The first two modes are theoretically equiprobable. In the dominant mode for the spanwise velocity component, Fig. 20(b), both upstream and downstream motions are detected but with also a nonhomogeneous spanwise movement at the cavity closure. Unlike the case with sidewalls, this mode is not symmetric and it highlights an alternation of the spanwise velocity component along the spanwise axis. Furthermore, the second mode has an opposite movement along the spanwise axis. The SPOD mode

behavior, for the streamwise and the vertical velocity components, is similar to the ones for the case with sidewalls.

## VIII. DISCUSSION

A dominant dynamics has been highlighted by diverse analysis of the cavitating flow. It has to be noticed that a similar behavior has been detected in computations with the turbulence model of Spalart Allmaras. The current section offers the authors interpretation of the phenomenon.

Oblique-shape behaviors of the cavitation pocket have already been observed in two different sheet cavitation experiments. The first one is a venturi flow experiment with  $8^\circ$  divergent angle carried out by Dular *et al.* (2012).<sup>28</sup> In this case, vapor release into the flow appears under certain conditions and, for one of the studied geometry, the cavity presents a nonsymmetrical shape. The authors suggest that it is caused by the re-entrant jet, which, besides going upstream, turns to the side. Nevertheless, due to the higher divergent angle, the pocket is cut by the re-entrant jet and leads to a vapor release. The second experiment is a flow around a guide vane profile carried out by Timoshevskiy *et al.* (2016).<sup>26</sup> Under the vapor release regime,

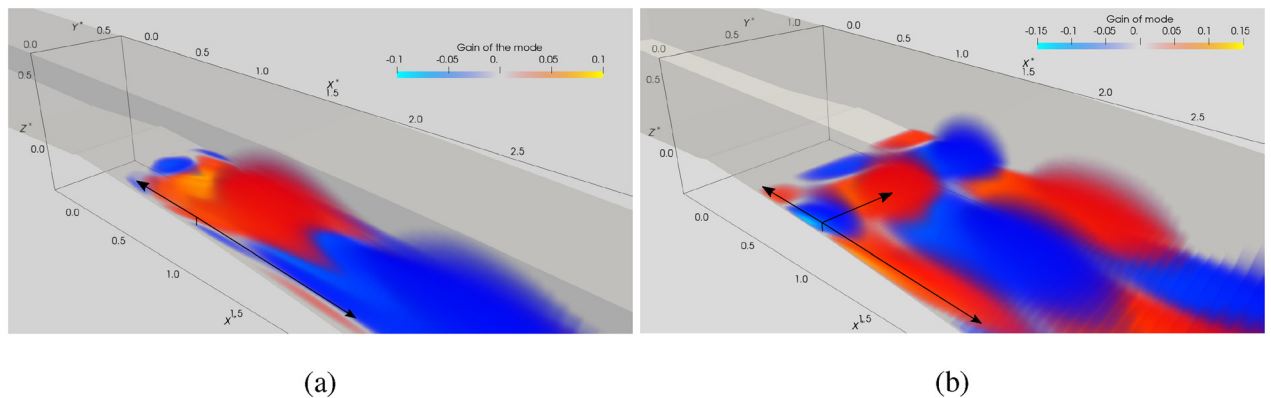


**FIG. 20.** Volume rendering of the dominant mode of the SPOD for  $v$  at  $St = 1.09$ ;  $\rightarrow$ : Time evolution behavior: (a) for the case with sidewalls and (b) for the case with periodic side boundaries.

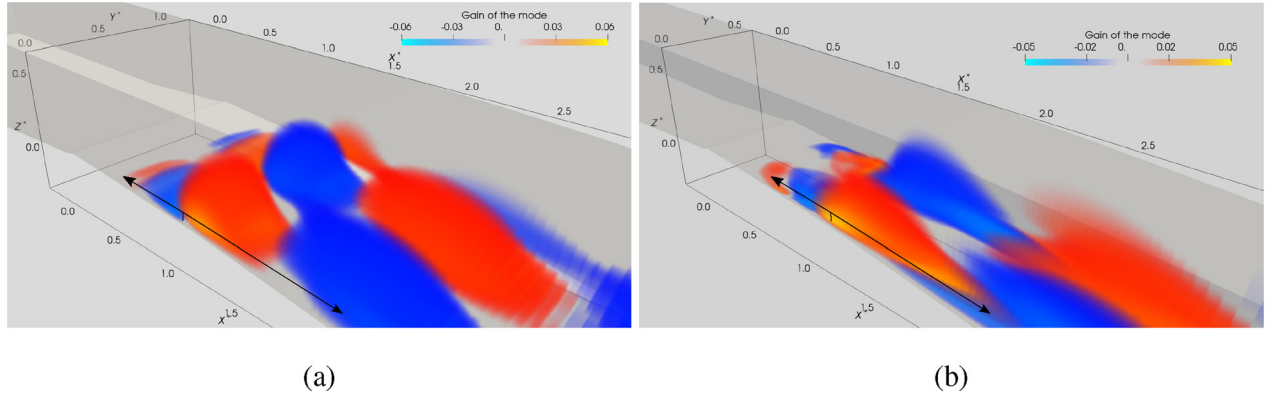


**FIG. 21.** Volume rendering of the dominant mode of the SPOD for  $w$  at  $St = 1.09$ ;  $\rightarrow$ : Time evolution behavior: (a) for the case with sidewalls and (b) for the case with periodic side boundaries.

nonsymmetrical cavitation pocket behavior appears, as for the previous experiment. However, this regime is defined as nonpersistent by the authors. Both experiments present a vapor release regime which could explain that the re-entrant jet bifurcation and the cavity shape do not lead to an identical spanwise oscillation. Nonetheless, it is suggested that the leading mechanism of those phenomena could be the same. The behavior of the re-entrant jet against the cavitation pocket in both experiments and the current work is identical: when the cavity is expanded on one side, the re-entrant jet is more developed on the other side.

The SPOD analysis validates the presence of a dominant dynamics of the flow at a Strouhal number of 1.09. First, for the case with sidewalls, such a phenomenon is associated with the spanwise oscillation of the flow. The re-entrant jet is then captured as observed in the mode dynamics for density and velocity components. For this reason, it presents a significant role in the spanwise oscillation. The present study does not give enough information to ensure that the re-entrant jet is the mechanism which leads to the oscillation. Nevertheless, experiments describing the vapor release regime considered that the shedding is triggered by the re-entrant jet which “cuts” the cavity by going upward. Therefore, given the promiscuity of the physical phenomenon, it can be presumed that the re-entrant jet is the leading mechanism of the oscillation for the present case.

The spanwise oscillation is easily observed through the dominant mode dynamics for the spanwise velocity, which highlights an alternation of positive and negative velocity around the cavity closure. By analyzing the predominant mode dynamics for the velocity components, it is noticed that the oscillation pattern is simultaneously propagated upstream, by the re-entrant jet, and downstream by the main flow. The downstream flow is thus highly influenced by the pocket and the re-entrant jet dynamics while the oscillation seems to be self-sustained by the upstream flow, suggesting the possible existence of a global mode driving this dynamic.

Fluctuations observed just downstream the cavitation pocket are interpreted as an oscillation of magnitude for the vertical and the streamwise velocity components. When the pocket is expanded near a sidewall, the magnitude of these two components is increased on the same side and decreased on the other. This information involves that the longer the cavity is, the more accelerated the downward and the

downstream speeds are. When the pocket moves to the other side, the velocity effects are reversed. Hence, the cavitation pocket interferes with the flow can be seen as a dynamic fluidic obstacle.

The results of the simulation with periodic side boundaries give relevant information about the sidewalls impact on the flow. For this case, the cavity and the re-entrant jet shapes are unchanged along the spanwise axis. Therefore, the U-shape of the cavitation pocket and the re-entrant jet shape are linked to the presence of sidewalls. However, the extraction of a dominant mode at the same Strouhal number suggests that the sidewalls do not trigger the spanwise oscillation but only amplify a phenomenon. The dominant dynamics is then led by a mechanism specific to the cavitating flow. The Strouhal number of 1.09 linked to the dominant mode is obtained by using two characteristic quantities: the length of the cavitation pocket  $L_c = 0.0788$  m and the maximum time-averaged velocity of the re-entrant jet at the mid-span  $u_{jet}^{max} = 2.38$  m s<sup>-1</sup>. Hence, the mechanism highlighted by the current study seems to be inherent to the pocket development.

For the periodic case, the associated energy of the two first SPOD modes extracted at the Strouhal number  $St_0$  is close. The impact of these modes on the flow is then almost identical. Furthermore, both present an opposite spanwise movement of the fluctuations for the density and the spanwise velocity component. The two modes could be described as a bifurcation of the flow with an equal probability of appearance. This hypothesis could be investigated by simulating the case on a much longer time.

## IX. CONCLUSION

The 3D effects of cavitating flow, with a partial cavity, are studied in the case of a 4° divergent angle venturi. Two configurations, with sidewalls and with periodic side boundaries, are computed for an identical physical time. Time-averaged data and dynamic analysis highlight flow structure differences, in particular, in the cavitation pocket and re-entrant-jet shapes. Nonetheless, an identical Strouhal number of 1.09 linked to flow fluctuations is extracted in both cases. The SPOD analysis provides details about this phenomenon. A dominant mode at this Strouhal number is captured for both cases. For the simulation with sidewalls, it represents a spanwise oscillation of the flow observed through the cavitation pocket and re-entrant jet oscillation. It is noticed that the cavity and the re-entrant jet oscillations are in

opposition of phase. Moreover, the flow bypassing the cavitation pocket accelerates and follows the pocket oscillation. Thus, the cavitation pocket acts as a dynamic obstacle. For the case with periodic spanwise boundaries, the dominant SPOD mode is energetically close to the second one at the same Strouhal number. Both show similar dynamics but with an opposite spanwise motion. These two modes could represent a flow bifurcation concerning spanwise fluctuations and are ideally equiprobable. Finally, the analysis of both cases involves that 3D effects, nonrelated to the presence of sidewalls, appear in this cavitating flow configuration. The results also suggest that the phenomenon is linked to two characteristic variables of the flow: the cavity length and the maximum of the time-averaged re-entrant jet velocity at midspan. The link between the extracted Strouhal number and the two characteristic variables could be investigated. Other flow configurations presenting distinct cavity length could be used to attest the robustness of this conclusion.

## ACKNOWLEDGMENTS

This research was supported by the French National Research Agency ANR (Project No. 18-CE46-009). This work was granted access to the HPC resources of IDRIS under the allocation 2020-A0072A06362 made by GENCI. The authors thank Jean-Christophe Loiseau for providing the SPOD code.

## APPENDIX: MODIFIED THIRD-ORDER JAMESON-SCHMIDT-TURKEL SCHEME

For stiff problems like sheet cavitation modeled with a 1-fluid method, centered schemes with artificial dissipation have been selected. The Jameson-Schmidt-Turkel (JST) scheme is a second-order scheme proposed by Jameson *et al.* (1981).<sup>67</sup> It is composed of a second-order centered scheme and a dissipation term

$$\mathbf{F}_{ci+\frac{1}{2}j} = \frac{1}{2}(\mathbf{F}_{ci+1j} + \mathbf{F}_{cij}) - D_{1+\frac{1}{2}j}(\mathbf{w}_{i+1j} - \mathbf{w}_{ij}). \quad (\text{A1})$$

In this 2D example, the flux is computed on the interface  $i + \frac{1}{2}$  in the x direction. The term  $D_1$  represents the dissipation separated in two parts. The first part is a second-order dissipation based on a pressure sensor  $\eta_i$  and the second part is a four-order dissipation. It can be written, for the current example, as

$$\begin{aligned} D_{i+\frac{1}{2}j}(\mathbf{w}_{i+1j} - \mathbf{w}_{ij}) &= \varepsilon_{i+\frac{1}{2}j}^{(2)} \rho(\mathbf{A}_{i+\frac{1}{2}j})(\mathbf{w}_{i+1j} - \mathbf{w}_{ij}) \\ &\quad - \varepsilon_{i+\frac{1}{2}j}^{(4)} \rho(\mathbf{A}_{i+\frac{1}{2}j})(\mathbf{w}_{i+2j} - 3\mathbf{w}_{i+1j} + 3\mathbf{w}_{ij} - \mathbf{w}_{i-1j}), \end{aligned} \quad (\text{A2})$$

with  $\rho(\mathbf{A}_{i+\frac{1}{2}j})$  the spectral radius of the Jacobian matrix  $\mathbf{A}$ . The term  $\varepsilon_{i+\frac{1}{2}j}^{(2)}$  is defined with a parameter  $k^{(2)} \in [0, 1]$  and the pressure sensor  $\eta_i$ ,

$$\begin{aligned} \varepsilon_{i+\frac{1}{2}j}^{(2)} &= k^{(2)} \max[\eta_i; \eta_{i+1}], \\ \eta_i &= \frac{|p_{i+1} - 2p_i + p_{i-1}|}{p_{i+1} + 2p_i + p_{i-1}}. \end{aligned}$$

This sensor allows triggering the second-order dissipation only around high pressure gradients. The term  $\varepsilon_{i+\frac{1}{2}j}^{(4)}$  is defined with a

parameter  $k^{(4)} \in [0.008, 0.064]$  and allows to damp small oscillation far from shocks,

$$\varepsilon_{i+\frac{1}{2}j}^{(4)} = \max\left[0, k^{(4)} - \varepsilon_{i+\frac{1}{2}j}^2\right].$$

Nevertheless, in the 1-fluid flow, high-density gradients appear along with the interface between liquid and vapor. To prevent computational problems, a third term is added to the dissipation with the same formula that the  $\varepsilon_{i+1/2,j}^{(2)}$  but with another sensor  $\eta_i^{(I)}$  based on the density,

$$\eta_i^{(I)} = \frac{|\rho_{i+1} - 2\rho_i + \rho_{i-1}|}{\rho_{i+1} + 2\rho_i + \rho_{i-1}}. \quad (\text{A3})$$

Hence, the dissipation term  $\varepsilon_{i+1/2,j}^{(2)}$  could be written as a sum of a dissipation around shocks and another around interface with their own constant  $k^{(2)}$  and  $k_i^{(2)}$ ,

$$\varepsilon_{i+1/2,j}^{(2)} = \varepsilon_{i+1/2,j}^{(2) \text{ shock}} + \varepsilon_{i+1/2,j}^{(2) \text{ interface}}.$$

Finally, the second-order centered scheme could be updated to a fourth-order one,

$$\mathbf{F}_{ci+\frac{1}{2}j} = \frac{1}{12}(-\mathbf{F}_{ci+2j} + 7\mathbf{F}_{ci+1j} + 7\mathbf{F}_{ci,j} - \mathbf{F}_{ci-1j}). \quad (\text{A4})$$

The global numerical scheme (centered part plus dissipation) is, therefore, a third-order one.

## DATA AVAILABILITY

The data that support the findings of this study are available from the corresponding author upon reasonable request.

## REFERENCES

- <sup>1</sup>K. R. Laberteaux and S. L. Ceccio, "Partial cavity flows. Part 1. Cavities forming on models without spanwise variation," *J. Fluid Mech.* **431**, 1–41 (2001).
- <sup>2</sup>D. F. de Lange, G. J. de Bruin, and L. van Wijngaarden, "On the mechanism of cloud cavitation - Experiment and modelling," in *Proceedings of Second International Symposium on Cavitation, CAV1994* (H. Kato, Tokyo, Japan, 1994), pp. 45–49.
- <sup>3</sup>Y. Kawanami, H. Kato, H. Yamaguchi, M. Tanimura, and Y. Tagaya, "Mechanism and control of cloud cavitation," *J. Fluids Eng.* **119**, 788–794 (1997).
- <sup>4</sup>G. Reisman, Y.-C. Wang, and C. Brennen, "Observations of shock waves in cloud cavitation," *J. Fluid Mech.* **355**, 255–283 (1998).
- <sup>5</sup>S. Gopalan and J. Katz, "Flow structure and modeling issues in the closure region of attached cavitation," *Phys. Fluids* **12**, 895 (2000).
- <sup>6</sup>M. Callenaere, J.-P. Franc, J.-M. Michel, and M. Riondet, "The cavitation instability induced by the development of a re-entrant jet," *J. Fluid Mech.* **444**, 223–256 (2001).
- <sup>7</sup>O. Coutier-Delgosha, J.-F. Devillers, and T. Pichon, "Internal structure and dynamics of sheet cavitation," *Phys. Fluids* **18**, 017103 (2006).
- <sup>8</sup>S. Hayashi and K. Sato, "Unsteady behavior of cavitating waterjet in an axisymmetric convergent-divergent nozzle: High speed observation and image analysis based on frame difference method," *J. Flow Control, Meas. Visualization* **2**, 94–104 (2014).
- <sup>9</sup>A. Y. Kravtsova, D. M. Markovich, K. S. Pervunin, M. V. Timoshevskii, and K. Hanjalic, "Cavitation on a semicircular leading-edge plate and NACA0015 hydrofoil: Visualization and velocity measurement," *Therm. Eng.* **61**, 1007–1014 (2014).
- <sup>10</sup>S. Jahangir, W. Hogendoorn, and C. Poelma, "Dynamics of partial cavitation in an axisymmetric converging-diverging nozzle," *Int. J. Multiphase Flow* **106**, 34–45 (2018).



- <sup>11</sup>R. A. E. Arndt, C. C. S. Song, M. K. J. He, and A. Keller, "Instability of partial cavitation: A numerical/experimental approach," in *Proceedings of Twenty-Third Symposium on Naval Hydrodynamics* (National Academies Press, 2000).
- <sup>12</sup>C. Stanley, T. Barber, B. Milton, and G. Rosengarten, "Periodic cavitation shedding in a cylindrical orifice," *Exp. Fluids* **51**, 1189–1200 (2011).
- <sup>13</sup>C. Stanley, T. Barber, and G. Rosengarten, "Re-entrant jet mechanism for periodic cavitation shedding in a cylindrical orifice," *Int. J. Heat Fluid Flow* **50**, 169–176 (2014).
- <sup>14</sup>H. Ganesh, S. A. Mäkiharju, and S. L. Ceccio, "Bubbly shock propagation as a mechanism for sheet-to-cloud transition of partial cavities," *J. Fluid Mech.* **802**, 37–78 (2016).
- <sup>15</sup>B. Charrière and E. Goncalves, "Numerical investigation of periodic cavitation shedding in a Venturi," *Int. J. Heat Fluid Flow* **64**, 41–54 (2017).
- <sup>16</sup>D. de Lange and G. de Bruin, "Sheet cavitation and cloud cavitation re-entrant jet and three-dimensionality," *Appl. Sci. Res.* **58**, 91–114 (1997).
- <sup>17</sup>E. J. Foeth, C. W. H. van Doorne, T. van Terwisga, and B. Wieneke, "Time resolved PIV and flow visualization of 3D sheet cavitation," *Exp. Fluids* **40**, 503–513 (2006).
- <sup>18</sup>M. Dular, R. Bachert, C. Schaad, and B. Stoffel, "Investigation of a re-entrant jet reflection at an inclined cavity closure line," *Eur. J. Mech.-B/Fluids* **26**, 688–705 (2007).
- <sup>19</sup>G. H. Schnerr, I. H. Sezal, and S. J. Schmid, "Numerical investigation of three-dimensional cloud cavitation with special emphasis on collapse induced shock dynamics," *Phys. Fluids* **20**, 040703 (2008).
- <sup>20</sup>A. Kubota, H. Kato, H. Yamaguchi, and M. Maeda, "Unsteady structure measurement of cloud cavitation on a foil section using conditional sampling technique," *J. Fluids Eng.* **111**, 204–210 (1989).
- <sup>21</sup>X. Peng, B. Ji, Y. Cao, L. Xu, G. Zhang, X. Luo, and X. Long, "Combined experimental observation and numerical simulation of the cloud cavitation with U-type flow structures on hydrofoils," *Int. J. Multiphase Flow* **79**, 10–22 (2016).
- <sup>22</sup>E. Kadivar, O. el Moctar, and K. Javadi, "Stabilization of cloud cavitation instabilities using cylindrical cavitating-bubble generators (CCGs)," *Int. J. Multiphase Flow* **115**, 108–125 (2019).
- <sup>23</sup>B. Che, L. Cao, N. Chu, D. Likhachev, and D. Wu, "Dynamic behaviors of re-entrant jet and cavity shedding during transitional cavity oscillation on NACA0015 hydrofoil," *J. Fluids Eng.* **141**, 061101 (2019).
- <sup>24</sup>X. Long, H. Cheng, B. Ji, R. E. Arndt, and X. Peng, "Large eddy simulation and Euler–Lagrangian coupling investigation of the transient cavitating turbulent flow around a twisted hydrofoil," *Int. J. Multiphase Flow* **100**, 41–56 (2018).
- <sup>25</sup>J. Decaix and E. Goncalves, "Investigation of three-dimensional effects on a cavitating Venturi flow," *Int. J. Heat Fluid Flow* **44**, 576–595 (2013).
- <sup>26</sup>M. V. Timoshevskiy, S. A. Churkin, A. Y. Kravtsova, K. S. Pervunin, D. M. Markovich, and K. Hanjalic, "Cavitating flow around a scaled-down model of guide vanes of a high-pressure turbine," *Int. J. Multiphase Flow* **78**, 75–87 (2016).
- <sup>27</sup>D. T. Kawakami, A. Fuji, Y. Tsujimoto, and R. E. A. Arndt, "An assessment of the influence of environmental factors on cavitation instabilities," *J. Fluids Eng.* **130**, 031303 (2008).
- <sup>28</sup>M. Dular, I. Khelifa, S. Fuzier, M. A. Maiga, and O. Coutier-Delgosha, "Scale effect on unsteady cloud cavitation," *Exp. Fluids* **53**, 1233–1250 (2012).
- <sup>29</sup>Y. Delannoy and J. Kueny, "Two phase flow approach in unsteady cavitation modelling," in *Proceedings of Cavitation and Multiphase Flow Forum, Spring Meeting* (American Society of Mechanical Engineers, Toronto, Canada, 1990), Vol. 98, pp. 153–158.
- <sup>30</sup>S. Clerc, "Numerical simulation of the homogeneous equilibrium model for two-phase flows," *J. Comput. Phys.* **161**, 354–375 (2000).
- <sup>31</sup>E. Sinibaldi, F. Beux, and M. Salvetti, "A numerical method for 3D barotropic flows in turbomachinery," *Flow, Turbul. Combust.* **76**, 371–381 (2006).
- <sup>32</sup>P. Downar-Zapolski, Z. Bilicki, L. Bolle, and J. Franco, "The non-equilibrium relaxation model for one-dimensional flashing liquid flow," *Int. J. Multiphase Flow* **22**, 473–483 (1996).
- <sup>33</sup>R. F. Kunz, D. A. Boger, D. R. Stinebring, T. S. Chyczewski, J. W. Lindau, H. J. Gibeling, S. Venkateswaran, and T. Govindan, "A preconditioned Navier–Stokes method for two-phase flows with application to cavitation prediction," *Comput. Fluids* **29**, 849–875 (2000).
- <sup>34</sup>P. J. Zwart, A. G. Gerber, and T. Belamri, "A two-phase flow model for predicting cavitation dynamics," in *Proceedings of International Conference on Multiphase Flow, Yokohama, Japan* (ICMF, 2004), Paper No. 12.
- <sup>35</sup>P. Helluy and N. Seguin, "Relaxation models of phase transition flows," *ESAIM: Math. Modell. Numer. Anal.* **40**, 331–352 (2006).
- <sup>36</sup>Y. Saito, R. Takami, I. Nakamori, and T. Ikohagi, "Numerical analysis of unsteady behavior of cloud cavitation around a NACA0015 foil," *Comput. Mech.* **40**, 85 (2007).
- <sup>37</sup>S. Park and S. H. Rhee, "Numerical analysis of the three-dimensional cloud cavitating flow around a twisted hydrofoil," *Fluid Dyn. Res.* **45**, 015502 (2013).
- <sup>38</sup>M. Sedlar, B. Ji, T. Kratky, T. Rebok, and R. Huzlik, "Numerical and experimental investigation of three-dimensional cavitating flow around the straight NACA2412 hydrofoil," *Ocean Eng.* **123**, 357–382 (2016).
- <sup>39</sup>V. Hidalgo, X. Escaler, E. Valencia, X. Peng, J. Erazo, D. Puga, and X. Luo, "Scale-adaptive simulation of unsteady cavitation around a NACA66 hydrofoil," *Appl. Sci.* **9**, 3696 (2019).
- <sup>40</sup>T. Sun, X. Zhang, C. Xu, G. Zhang, and S. Jiang, "Numerical modeling and simulation of the shedding mechanism and vortex structures at the development stage of ventilated partial cavitating flows," *Eur. J. Mech.-B/Fluids* **76**, 223–232 (2019).
- <sup>41</sup>B. Ji, X. Luo, Y. Wu, X. Peng, and Y. Duan, "Numerical analysis of unsteady cavitating turbulent flow and shedding horse-shoe vortex structure around a twisted hydrofoil," *Int. J. Multiphase Flow* **51**, 33–43 (2013).
- <sup>42</sup>B. Huang, Y. Zhao, and G. Wang, "Large eddy simulation of turbulent vortex-cavitation interactions in transient sheet/cloud cavitating flows," *Comput. Fluids* **92**, 113–124 (2014).
- <sup>43</sup>B. Ji, X.-w. Luo, X.-x. Peng, and Y.-l. Wu, "Three-dimensional large eddy simulation and vorticity analysis of unsteady cavitating flow around a twisted hydrofoil," *J. Hydrodyn.* **25**, 510–519 (2013).
- <sup>44</sup>A. Gnanaskandan and K. Mahesh, "Large eddy simulation of the transition from sheet to cloud cavitation over a wedge," *Int. J. Multiphase Flow* **83**, 86–102 (2016).
- <sup>45</sup>Y. Chen, J. Li, Z. Gong, X. Chen, and C. Lu, "Large eddy simulation and investigation on the laminar-turbulent transition and turbulence-cavitation interaction in the cavitating flow around hydrofoil," *Int. J. Multiphase Flow* **112**, 300–322 (2019).
- <sup>46</sup>T. Sun, Z. Wang, L. Zou, and H. Wang, "Numerical investigation of positive effects of ventilated cavitation around a NACA66 hydrofoil," *Ocean Eng.* **197**, 106831 (2020).
- <sup>47</sup>C. P. Egerer, S. Hickel, S. J. Schmidt, and N. A. Adams, "Large-eddy simulation of turbulent cavitating flow in a micro channel," *Phys. Fluids* **26**, 085102 (2014).
- <sup>48</sup>S. Barre, J. Rolland, G. Boitel, E. Goncalves, and R. F. Patella, "Experiments and modeling of cavitating flows in Venturi: Attached sheet cavitation," *Eur. J. Mech.-B/Fluids* **28**, 444–464 (2009).
- <sup>49</sup>C. Merkle, J. Feng, and P. Buelow, "Computation modeling of the dynamics of sheet cavitation," in *Proceedings of 3rd International Symposium on Cavitation CAV1998*, Grenoble, France (1998).
- <sup>50</sup>B. Smith, "The  $k - \ell$  turbulence model and wall layer model for compressible flows," AIAA Paper No. 90–1483, 1990.
- <sup>51</sup>B. Smith, "A near wall model for the  $k - \ell$  two equation turbulence model," AIAA Paper No. 94–2386, 1994.
- <sup>52</sup>E. Goncalves and J. Decaix, "Wall model and mesh influence study for partial cavities," *Eur. J. Mech.-B/Fluids* **31**, 12–29 (2012).
- <sup>53</sup>B. Charrière, J. Decaix, and E. Goncalves, "A comparative study of cavitation model in a Venturi flow," *Eur. J. Mech.-B/Fluids* **49**, 287–297 (2015).
- <sup>54</sup>J.-L. Reboud, B. Stutz, and O. Coutier, "Two-phase flow structure of cavitation: Experiment and modelling of unsteady effects," in *Proceedings of 3rd International Symposium on Cavitation CAV1998*, Grenoble, France (1998).
- <sup>55</sup>J. Decaix and E. Goncalves, "Time-dependent simulation of cavitating flow with  $k - \ell$  turbulence models," *Int. J. Numer. Methods Fluids* **68**, 1053–1072 (2012).
- <sup>56</sup>J. Dandois, "Improvement of corner flow prediction using the quadratic constitutive relation," *AIAA J.* **52**, 2795 (2014).
- <sup>57</sup>P. R. Spalart, "Strategies for turbulence modelling and simulations," *Int. J. Heat Fluid Flow* **21**, 252–263 (2000).
- <sup>58</sup>R. Saurer, F. Petitpas, and R. Abgrall, "Modelling phase transition in metastable liquids: Application to cavitating and flashing flows," *J. Fluid Mech.* **607**, 313–350 (2008).

- <sup>59</sup>E. Goncalvès, “Numerical study of expansion tube problems: Towards the simulation of cavitation,” *Comput. Fluids* **72**, 1–19 (2013).
- <sup>60</sup>G. Wallis, *One-Dimensional Two-Phase Flow* (McGraw-Hill, NY, 1967).
- <sup>61</sup>B. Charrière, “Modélisation et simulation d’écoulements turbulents cavitants avec un modèle de transport de taux de vide; in English: Modelling and simulation of cavitating turbulent flows using a transport equation of void ratio,” Ph.D. thesis (Université Grenoble Alpes, Laboratoire Des Écoulements Géophysiques et Industrielles, Grenoble, France, 2015).
- <sup>62</sup>E. Goncalves and R. F. Patella, “Numerical simulation of cavitating flows with homogeneous models,” *Comput. Fluids* **38**, 1682–1696 (2009).
- <sup>63</sup>E. Turkel, “Preconditioned methods for solving the incompressible and low speed compressible equations,” *J. Comput. Phys.* **72**, 277–298 (1987).
- <sup>64</sup>Y. Choi and C. Merkle, “The application of preconditioning to viscous flows,” *J. Comput. Phys.* **105**, 207–223 (1993).
- <sup>65</sup>R. J. Spiteri and S. J. Ruuth, “A new class of optimal high-order strong-stability-preserving time discretization methods,” *SIAM J. Numer. Anal.* **40**, 469–491 (2002).
- <sup>66</sup>S. Gottlieb, “On high order strong stability preserving Runge–Kutta and multi step time discretizations,” *J. Sci. Comput.* **25**, 105–128 (2005).
- <sup>67</sup>A. Jameson, W. Schmidt, and E. Turkel, “Numerical solutions of the Euler equations by finite volume methods using Runge–Kutta time-stepping schemes,” AIAA Paper No. 81–1259, 1981.
- <sup>68</sup>E. Goncalvès and B. Charrière, “Modelling for isothermal cavitation with a four-equation model,” *Int. J. Multiphase Flow* **59**, 54–72 (2014).
- <sup>69</sup>E. Goncalves and D. Zeidan, “Simulation of compressible two-phase flows using a void ratio transport equation,” *Commun. Comput. Phys.* **24**, 167–203 (2018).
- <sup>70</sup>L. Zhou and Z. Wang, “Numerical simulation of cavitation around a hydrofoil and evaluation of a RNG k-epsilon model,” *J. Fluids Eng.* **130**, 011302 (2008).
- <sup>71</sup>A. Ducoin, B. Huang, and Y. Young, “Numerical modeling of unsteady cavitating flows around a stationary hydrofoil,” *Int. J. Rotating Mach.* **2012**, 215678.
- <sup>72</sup>B. Ji, X. Luo, R. Arndt, and Y. Wu, “Numerical simulation of three dimensional cavitation shedding dynamics with special emphasis on cavitation-vortex interaction,” *Ocean Eng.* **87**, 64–77 (2014).
- <sup>73</sup>M. Dular and R. Bachert, “The issue of Strouhal number definition in cavitating flow,” *J. Mech. Eng.* **55**, 666–674 (2009).
- <sup>74</sup>D. Hammond and L. Redekopp, “Local and global instability properties of separation bubbles,” *Eur. J. Mech.-B/Fluids* **17**, 145–164 (1998).
- <sup>75</sup>U. Rist and U. Maucher, “Investigations of time-growing instabilities in laminar separation bubbles,” *Eur. J. Mech.-B/Fluids* **21**, 495–509 (2002).
- <sup>76</sup>A. Gnanaskandan and K. Mahesh, “Numerical investigation of near-wake characteristics of cavitating flow over a circular cylinder,” *J. Fluid Mech.* **790**, 453–491 (2016).
- <sup>77</sup>B. Budich, S. J. Schmidt, and N. A. Adams, “Numerical simulation and analysis of condensation shock in cavitating flow,” *J. Fluid Mech.* **838**, 759–813 (2018).
- <sup>78</sup>A. Towne, O. T. Schmidt, and T. Colonius, “Spectral proper orthogonal decomposition and its relationship to dynamic mode decomposition and resolvent analysis,” *J. Fluid Mech.* **847**, 821–867 (2018).
- <sup>79</sup>O. T. Schmidt and T. Colonius, “Guide to spectral proper orthogonal decomposition,” *AIAA J.* **58**, 1023 (2020).
- <sup>80</sup>B. Chu, “On the energy transfer to small disturbances in fluid flow (Part I),” *Acta Mech.* **1**, 215–234 (1965).